A Generalized Mixed-Cell Method for Eulerian Network Transport Modeling

Toko Kamtchueng[1], Adil Mohammed Sbai[2], Jean-Louis Rouet[3], Olivier Rozenbaum[3], and Mohamed Azaroual[4]

[1]BRGM
[2]BRGM (French Geological Qurvey)
[3]Université d'Orléans
[4]Bureau de Recherches Geolog. et Minieres

November 22, 2022

Abstract

Pore network models are efficient tools for upscaling flow and transport properties in porous media. This work introduces a new formal mathematical derivation of the discrete equations governing solute transport in a pore network model. A double Laplace transform technique is applied by enforcing mass flux continuity along with the interfaces between pores and throats. A non-local semi-analytical formulation results. Solutions are given as a sum of convolution products with time-dependent and exponentially decaying local Péclet-dependent infinite series. Continuous concentration profiles along throats are calculated analytically, a posteriori, from time-dependent numerically simulated concentrations in pores. The upwind and central-difference schemes of the widely used mixed-cell method are found to be equivalent to the asymptotic form of this new formulation for the advective and diffusive dominant regimes, respectively. Therefore, the validity range of these static methods is established. The model was compared to the delay differential equations approach, a newly derived analytical solution, and mixed-cell methods on idealized one-dimensional networks eliminating topological disorder. Concentrations in pores are best reproduced when transport in the throats is not neglected unlike for the mixed-cell method leading to early breakthrough and first-order moment. An efficient numerical scheme truncating the encoded memory effects in the convolution kernels is introduced. This paves the way for the model application to realistic networks extracted from digital rock images. We caution against using static formulations as the error can be very large locally before attending a steady-state.

A Generalized Mixed-Cell Method for Eulerian Network Transport Modeling

T. Kamtchueng[1], **M. A. Sbai**[1], **J. L. Rouet**[2], **O. Rozenbaum**[2], **M. Azaroual**[1,2]

[1]BRGM (French Geological Survey), Avenue Claude Guillemin, 45060, BP 36009, Orléans Cedex 2, France
[2]Université d'Orléans, ISTO UMR 7327, Campus Géosciences, 1A Rue de la Férollerie, 45100, Orléans Cedex 2, France

Key Points:

- Novel non-local semi-analytical formulation for modeling solute transport in pore networks
- Mixed-cell methods are end members of the asymptotic general formulation for advective and diffusive dominant regimes
- Numerical solutions compared favorably with our new analytical solution and the delay differential equations approach

Corresponding author: M. A. Sbai, `sbai.adil@gmail.com; a.sbai@brgm.fr`

Abstract

Pore network models are efficient tools for upscaling flow and transport properties in porous media. This work introduces a new formal mathematical derivation of the discrete equations governing solute transport in a pore network model. A double Laplace transform technique is applied by enforcing mass flux continuity along with the interfaces between pores and throats. A non-local semi-analytical formulation results. Solutions are given as a sum of convolution products with time-dependent and exponentially decaying local Péclet-dependent infinite series. Continuous concentration profiles along throats are calculated analytically, a posteriori, from time-dependent numerically simulated concentrations in pores. The upwind and central-difference schemes of the widely used mixed-cell method are found to be equivalent to the asymptotic form of this new formulation for the advective and diffusive dominant regimes, respectively. Therefore, the validity range of these static methods is established. The model was compared to the delay differential equations approach, a newly derived analytical solution, and mixed-cell methods on idealized one-dimensional networks eliminating topological disorder. Concentrations in pores are best reproduced when transport in the throats is not neglected unlike for the mixed-cell method leading to early breakthrough and first-order moment. An efficient numerical scheme truncating the encoded memory effects in the convolution kernels is introduced. This paves the way for the model application to realistic networks extracted from digital rock images. We caution against using static formulations as the error can be very large locally before attending a steady-state.

1 Introduction

Accurately predicting solute transport migration at multiple scales in subsurface aquifers is identified among urgent societal and scientific challenges in water resources engineering, environmental pollution, and underground energy storage (Miller et al., 2013). Indeed, at the pore-scale, a porous medium lends itself to a random distribution of interconnected void space of non-uniform shape (Scheidegger, 1974; Dullien, 1992). At the representative elementary volume (REV) scale (Bear, 1972), however, this detailed pore-scale description is lumped into fundamental macroscopic flow and transport properties commonly used in current state-of-the-practice. These are, for instance, components of the intrinsic permeability and the hydrodynamic dispersion tensors governing the macroscopic behavior of solute transport. There is an overwhelming experimental and field evidence of solute dispersion dependence on the scale of observation as consistently documented in the literature (Anderson & Cherry, 1979; Pickens & Grisak, 1981; Sudicky et al., 1985; Silliman & Simpson, 1987; Silliman et al., 1987; Neuman, 1990; Schulze-Makuch, 2005). Gelhar et al. (1992) have reviewed observations from 59 field sites and concluded a high dependence of the longitudinal dispersivity on the observation scale. They indicated a variability range over six orders of magnitude (between 10^{-2} m and 10^{4} m) for scales ranging between 10^{-1} m and 10^{5} m, respectively. This field data-driven approach carries out several limitations because it does not translate the mechanistic impacts of pore-scale variability on the emergence of macroscopic transport mechanisms. In other words, it ignores the multiscale nature of solute transport processes. In order to make reliable predictions of subsurface flow and transport at the scales of interest, accurate and efficient numerical models need to be introduced. In particular, pore-scale models are essential tools to bridge the gap between the mechanistic processes occurring at the microscopic scale and their observable macroscopic manifestation at the REV scale. This is essential to understand how the pore-structure details control the transport processes for engineering applications.

Various numerical techniques such as the Lattice-Boltzmann (LB) method (Chen & Doolen, 1998; Yoon et al., 2015), the smoothed particle hydrodynamics (SPH) (Monaghan, 1992; Tartakovsky & Meakin, 2006; Tartakovsky et al., 2008), finite element (FE) (Zaretskiy et al., 2010; Bastian et al., 2011), and finite volume (FV) based computational fluid dynamics (CFD) methods (Molins et al., 2012; Icardi et al., 2014; Trebotich et al., 2014; Molins, 2015) have been used for the simulation of flow and solute transport in porous media at the pore-scale. All these simulation techniques are classified as direct approaches as they process directly the void space of the microstructure (Zaretskiy et al., 2010; Molins et al., 2012; Mostaghimi et al., 2012; Raeini et al., 2014, 2015). For instance FV and FE methods are Eulerian, the SPH technique is Lagrangian based, while LB is a kinetically based method (Chen & Doolen, 1998). As concluded from a recent inter-comparison study of pore-scale solute transport methods on two-dimensional micro-model experiments (Oostrom et al., 2016) and three-dimensional sphere packs (Yang et al., 2016), direct simulation methods require higher computational resources despite their high fidelity and accuracy. Limitations associated to the length scale that could be processed using direct approaches have made network modeling a very popular efficient alternative. Additionally, within pore network modeling it is more straightforward to incrementally support additional mass transport processes for applications of practical interest such as denitrification (Laudone et al., 2011), non-aqueous phase liquid dissolution (Dillard & Blunt, 2000), electrokinetic remediation (S. Li et al., 2014), geochemical wellbore cement carbonation (Raoof et al., 2012), biological clogging (Thullner & Baveye, 2008), carbonate matrix acidizing (Fredd & Fogler, 1998; Budek & Szymczak, 2012; Tansey & Balhoff, 2016), and the mechanisms of particle fines transport, release, and capture (Sharma & Yortsos, 1987).

Network modeling in interconnected capillary ducts was pioneered by Fatt (1956a, 1956b, 1956c) to upscale relative permeability of immiscible two-phase flow using volumeless pores and throats with distributed sizes. It seems, however, that the first reported use of three-dimensional pore networks goes back to Owen (1952) who investigated the relationship between a porous medium resistivity and pore space geometry. Those earlier models represent a dramatic shift from the simplest depiction of porous media as a bundle of capillary tubes of arbitrarily varying diameters failing to reproduce experimental observations. For more than five decades later, it is recognized that current state-of-the-art multiphase flow network models are predictive (Blunt, 2001; Blunt et al., 2013) if the network topological and geometrical properties are preserved during network extraction from pore space images (Blunt et al., 2013). Compared to recent advances in multiphase fluid flow, there is much less progress targeting network modeling of solute transport. Nowadays, there is a strong regain of interest in network modeling as a direct consequence of sustained rapid progress of non-invasive three-dimensional synchrotron X-ray micro-tomographic imaging (micro-CT) (Blunt et al., 2013; Wildenschild & Sheppard, 2013) and nuclear magnetic resonance spectroscopy (Song et al., 2008) instrumentations. The obtained images drive topological and morphological information on the porous media and so transport properties can be deduced using numerical tools. As these technologies are becoming almost a routine, opportunities to successful quantitative prediction of observations by pore-scale modeling are turning out from hope to foreseeable confidence.

Existing mass transport network models broadly belong to two main categories. First, in Lagrangian based models solute dispersion behavior in the rock is determined from a Markovian random walk process related to a brownian motion of a large number of massless particles. During their individual displacement, particles stochastically jump between streamlines in the transverse flow direction only (Sahimi et al., 1983, 1986) or in transverse and longitudinal directions (Sorbie & Clifford, 1991; Bijeljic et al., 2004). Second, Eulerian network models solve instead directly a discrete set of mass balance equations at the network elements. Popular formulations in this category rely on a set of mass balance equations given at all pores but not in the throats. These are the so-called mixed-cell methods (MCM) (Acharya et al., 2005, 2007; L. Li et al., 2006, 2008; Kim et al., 2011; Mehmani et al., 2012). This approach is so popular because it is simple to implement and efficient. There exist many numerical variants of this approach. The most frequent in the literature are based on a first-order upwind finite difference like scheme (Acharya et al., 2005; Raoof et al., 2012; S. Li et al., 2014; Mehmani et al., 2014; Qin et al., 2016; Tansey & Balhoff, 2016; Sadeghi et al., 2020). The second-order central difference scheme was also adopted in several works (Mehmani et al., 2012; Xiong et al., 2015, 2016). The latter is known to be stable only for moderate Péclet numbers. Sadeghi et al. (2020) have introduced three alternative formulations inspired from the CFD literature including a hybrid scheme, a power-law scheme, and an exponential scheme. Their work acknowledges the inaccuracy of the upwind MCM scheme whereas the exponential scheme was the most accurate when confronted to direct numerical simulations. A common drawback of all these network modeling approaches is that they are basically static and not time-dependent. It is actually unclear whether these methods are reliable tools for modeling dispersion in pore networks. Furthermore, these methods lack a defensible mathematical background as the underlying numerical schemes are questionably borrowed from those developed for solute transport at the continuum scale (Zheng & Bennett, 2002; Bear & Cheng, 2010).

Because MCM formulations overlook solute mass balance in throats alternative approaches have been sought. For instance, Raoof et al. (2013) have considered a modified mass balance equation on each pore. The concentration in each throat was linearly related to concentrations in its pore neighbors. Next, this relationship was substituted into the pores mass balance equations. Milligen and Bons (2014) have proposed an analytical expression of the mass flux in each throat assuming plug flow. Another method allowing to take into account the non-uniformity of the concentration in the network elements, including the pores and the throats, was given by Algive et al. (2010); Varloteaux et al. (2013). In their work, the moments theory was used to upscale the effective transport parameters assuming an asymptotic regime. Another previously developed approach adds additional degrees of freedom positions along each throat to accurately capture the concentration gradient. This method was proposed to simulate bioclogging in channels of a two-dimensional regular network by resorting to a finite difference scheme (Suchomel et al., 1998). This approach becomes cumbersome and intractable for realistic three-dimensional networks. Indeed, increased resolution in the throats is strategic for many applications involving a change in its geometric properties such as clogging, salt/mineral precipitation/dissolution reactions (L. Li et al., 2006, 2008; Raoof et al., 2012; Xiong et al., 2016), just to name a few. Notably, while all these alternative formulations acknowledge solute transport in the throats they are all static, which contradicts the endeavor of pore-scale modeling. Because these solute transport dynamics are fundamentally ignored or artificially repaired in the throats by the standard MCM formulation and its derivatives, a general dynamic formulation is lacking.

Until now, only two previously published works have considered the non-local effects when modeling solute transport by Eulerian network models. Martins et al. (2009) have indicated that non-local effects in porous media are manifested by the dependence of the pore concentration on the concentration history in other pores. They have formulated the problem as a delay differential equations system where the delay explicitly depends on the local characteristics of each throat. This model is limited, however, to a purely advective regime. Mehmani and Balhoff (2015a) performed space-time convolutions with semi-empirical elementary throat response functions calibrated with CFD simulations. Their method was shown to incorporate shear dispersion effects in throats by reproducing experimental data of longitudinal dispersion. It is, however, unclear how all these methods relate to each other. Thus, the objective of this paper is to challenge this issue by providing a generalized approach establishing a formal link between all MCM models and their derivatives.

The paper outline is as follows: section 2 recalls how local fluid velocities and flow rates are computed in a pore network. In section 3, the discrete form of mass balance equations in pores and throats will be presented. Using a double Laplace transform for the two sets of mass balance equations general expressions are derived in Laplace space. Using an analytical inverse Laplace transform technique, novel relationships expressing concentration behavior in network elements are derived. This will enable understanding the link between the different methods from the literature. Next, an accelerated numerical scheme is introduced to efficiently solve the underlying linear systems. The model is compared with the upwind MCM and the delay differential equations approaches establishing its performance. In particular, a demonstrative application on a realistic network extracted from a reconstructed three-dimensional pore space image highlights the inherent shortcomings of the asymptotic approaches. Finally, concluding remarks close the paper.

2 Fluid Flow Simulation in a Pore Network

Let us consider the pore network model (PNM) as a collection of a total number of n_p interconnected pores with n_t throats of distributed sizes (Figure 1). A PNM is a simplified representation of the porous media geometry enabling an analytic description of local flow and transport processes. We further assume, without loss of generality, that each throat has a constant cross-section. A saturated steady-state flow field in this network is established along the x-direction by imposing a pressure gradient $\Delta p = p_1 - p_2$ across the two x-orthogonal faces of the sample as illustrated in Figure 1. For an incompressible fluid, volume conservation implies that the algebraic sum of discharge rates at all throats meeting at pore i is zero, such that

$$\sum_{j=1}^{z_i} Q_{ij} = 0 \tag{1}$$

where Q_{ij} is the local flow rate between pores i and j, z_i is the coordination number of pore i. Equation 1 is the hydraulic analog to Kirchhoff's nodal rule in electrical engineering where the algebraic sum of currents in a network of resistors meeting at a point is null.

For a creeping flow regime at low Reynolds numbers (Re $\ll 1$) inertial forces are negligible compared to viscous forces and the flow rate is related to average pore pressure by the pore-scale constitutive relationship

$$Q_{ij} = \frac{g_{ij}}{l_{ij}} \left(p_i - p_j\right) \tag{2}$$

where g_{ij} and l_{ij} are the saturated hydraulic conductance and the total length of the throat ij, respectively (Figure 2). p_i is the pore pressure at node number i. The hydraulic conductance is approximated as the harmonic mean of each individual conductance weighted by their length as illustrated in Figure 2, such that

$$\frac{l_{ij}}{g_{ij}} = \frac{l_i}{g_i} + \frac{l_j}{g_j} + \frac{l_t}{g_t} \tag{3}$$

where l_i is the half-length of pore i and l_t is the strict length of the throat.

Pore network geometries are characterized by their shape factor G (Mason & Morrow, 1991) as the ratio of the sectional area S to the square of perimeter length. There is no hypothesis on the shape of the network throats cross-sections as they may have circular, triangular, or square shapes. When considering laminar flow through a cylindrical pipe of constant cross-section, its hydraulic conductance is given according to the Hagen-Poiseuille equation

$$g_t = G_f \frac{S^2 G}{\mu} \tag{4}$$

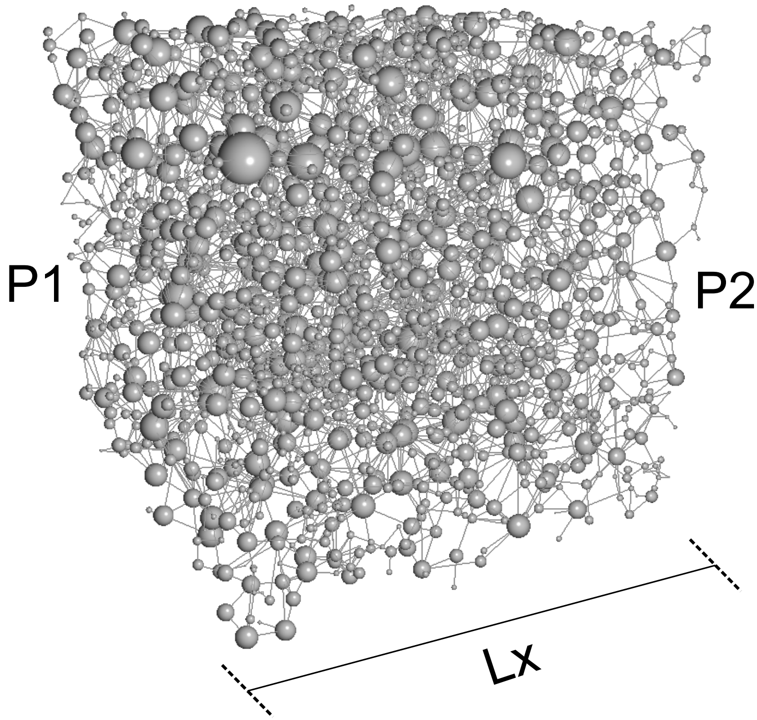

Figure 1. Example of a pore network model (PNM) of a sandstone porous medium with distributed elements sizes. Pore volume is proportional to sphere size. Prescribed pressures at inflowing/outflowing boundaries for modeling single-phase fluid flow are equally shown.

where μ is the dynamic viscosity of the fluid. The shape factor multiplier, G_f, value equals 0.5, 0.6, and 0.5623 for circular, equilateral triangles and squares, respectively (Patzek & Silin, 2001). Inserting equation 2 into equation 1 yields

$$\sum_{j=1}^{z_i} \frac{g_{ij}}{l_{ij}} (p_i - p_j) = 0 \tag{5}$$

Once the pressure field in all internal pores is calculated, fluid velocities $U = Q_{ij}/S$ in all network connections are simply post-processed by direct application of equation 2. By assuming also that the network size is sufficient for a REV description of a porous medium (Bear, 1972) we can calculate the macroscopic water velocity, v_x, along the x-direction in the network as

$$v_x = \frac{L_x}{V_T} Q_{out} = \frac{L_x}{V_T} \sum_{\Gamma_{out}} Q_{ij} \tag{6}$$

where L_x is the network length parallel to x-direction, V_T is the total volume of the network including all pores and throats, Q_{out} is the outflow rate at the exit boundary Γ_{out}. By simple application of Darcy's law it is straightforward to calculate the equivalent saturated permeability of the network in x-direction, k_x, from the following relationships

$$k_x = \frac{\mu L_x^2}{V_T \Delta p} Q_{out} \tag{7}$$

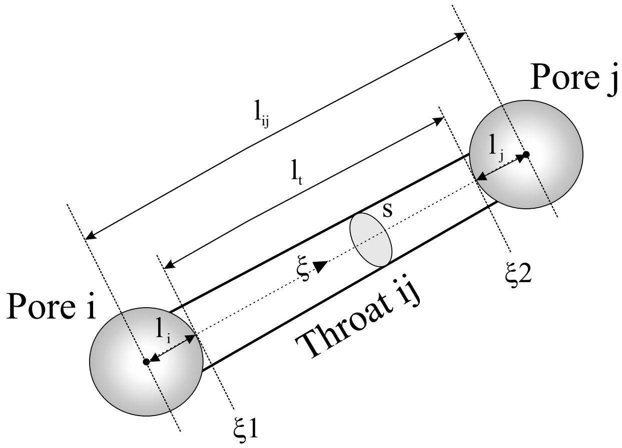

Figure 2. Schematic view of pore half-lengths l_i, l_j, the strict throat length l_t, and the total throat length for a pore-throat-pore assembly.

Finally, by sweeping the same applied pressure gradient across the faces orthogonal to y and z directions we can quantitatively estimate the diagonal upscaled permeability tensor $\mathbf{k} = diag(k_x, k_y, k_z)$ as a function of network geometrical and topological properties.

3 Semi-Analytical Solute Transport Solutions in a Pore Network

The rationale of approximating the pore space with a segmented pore network is to reduce the complexity and higher computational demands associated with direct methods. The principal ingredient of this approach is the coexistence of two interconnected basic entities corresponding to the so-called pores and throats corresponding to large and narrow portions of the void space, respectively. Most previous Eulerian pore network models considered a single mass balance in the pores to calculate the concentration evolution inside the network. In this section taking into account the geometrical simplification induced by the PNM approach, we integrate analytically the model and derive a new mathematical formulation to address this limitation.

3.1 Governing Solute Transport Equations

Assuming an incompressible stationary flow regime of a newtonian non-reactive viscous fluid in a porous medium, the equation governing mass transport in all elements of the network is given by

$$\frac{\partial c(\overrightarrow{r},t)}{\partial t} = -\mathbf{u}(\overrightarrow{r},t) \cdot \nabla c(\overrightarrow{r},t) + D\Delta c(\overrightarrow{r},t) \tag{8}$$

where $c(\overrightarrow{r},t)$ is the local solute concentration, $\mathbf{u}$ is the pore-scale fluid velocity, and D is the solute diffusivity. D is nothing more than the molecular diffusion coefficient D_m in pores.

3.1.1 Solute transport equations in pores

Integrating equation 8 on the i^{th} pore whose mean concentration at time t is $C_i(t)$ gives

$$V_i \frac{\partial C_i}{\partial t}(t) = -\int_{\Gamma_i} (\mathbf{u}c(\overrightarrow{r},t) - D\nabla c(\overrightarrow{r},t)) \cdot \mathbf{n}\, d\Gamma_i \tag{9}$$

where V_i is the volume of pore i, Γ_i is the union of solid-fluid Γ_s and fluid-fluid Γ_l interfaces at pore i. Notably, chemical surface reactions are not taken into account (i.e. $\mathbf{u}c - D\nabla c = 0 \quad \text{on} \quad \Gamma_s$). Hence, equation 9 is simply rewritten as

$$\begin{aligned} V_i \frac{\partial C_i}{\partial t} &= \sum_{l^+} \int_{\Gamma_l} (\mathbf{u}C - D\nabla C) \cdot \mathbf{n} \, d\Gamma_l \\ &\quad - \sum_{l^-} \int_{\Gamma_l} (\mathbf{u}C - D\nabla C) \cdot \mathbf{n} \, d\Gamma_l \end{aligned} \tag{10}$$

where Γ_l is the union of all fluid-fluid interfaces between a pore and its adjacent throats. l^+ and l^- denote filling and draining throats, respectively. By respectively introducing upstream and downstream total mass fluxes at fluid interfaces Γ_l denoted by J_l^+ and J_l^-, equation 10 becomes

$$V_i \frac{\partial C_i}{\partial t} = \sum_{l^+} J_l^+ \Gamma_l^+ - \sum_{l^-} J_l^- \Gamma_l^- \tag{11}$$

The left-hand side term quantifies solute accumulation inside the pore, while the right-hand side terms represent upstream (positive) and downstream (negative) total mass fluxes from adjacent throats, respectively.

3.1.2 Solute transport equations in throats

Consider a throat of length l, its cross-section is implicitly defined by the function S as schematically depicted in Figure 2. Because the fluid velocity in the throat is independent on its curvilinear position, mass transport in the throat is governed by the following one-dimensional convection-diffusion equation

$$\frac{\partial C}{\partial t}(\xi, t) = -U \frac{\partial C}{\partial \xi}(\xi, t) + D \frac{\partial^2 C}{\partial \xi^2}(\xi, t) \tag{12}$$

where U and C are the average velocity and concentration on a cross-section of a throat. Inside the throats D may be approximated according to the Taylor (1953) and Aris and Taylor (1956) theory for cylinders with moderate to high Péclet regimes. We further approximate upstream and downstream total mass fluxes at positions $\xi_1 = 0$ and $\xi_2 = l$, respectively, by the following relationships

$$J_{\xi_1}^-(t) \cong J(0, t) = UC(0, t) - D \frac{\partial C}{\partial \xi}(0, t) \tag{13}$$

$$J_{\xi_2}^+(t) \cong J(l, t) = UC(l, t) - D \frac{\partial C}{\partial \xi}(l, t) \tag{14}$$

To be in line with notation conventions introduced previously, the total mass fluxes $J_{\xi_1}^-(t)$ and $J_{\xi_2}^+(t)$ are considered to be downstream (negative) and upstream (positive) fluxes with respect to each pore neighbor. Note that $J_{\xi_1}^-(t)$ and $J_{\xi_2}^+(t)$ are only approximations to exact values of $J(0, t)$ and $J(l, t)$, respectively, because equation 12 is only an approximation to equation 8 in the throats.

3.2 Solute Transport Solutions in the Laplace Domain

To solve equations 11 and 12 subject to initial and boundary conditions, we use the Laplace transform method to derive a new semi-analytical formulation. Therefore, in this subsection we start first by deriving Laplace transforms, $\mathscr{L}$, of these two governing solute transport equations. Based on the definition of the Laplace transform for a real-time domain function $f(t)$

$$\bar{f}(s) = \mathscr{L}(f(t)) = \lim_{\tau \to +\infty} \int_0^\tau e^{-st} f(t) \, dt \tag{15}$$

Equations 11 and 12 will be rewritten in Laplace space resulting literally into linear algebraic equations and linear differential equations, respectively. Additionally, we derive analytical expressions, in the Laplace domain, of the total mass flux at the end positions of any throat.

3.2.1 Solute concentration in throats

Assuming zero initial concentration in the whole network, equation 12 is rewritten in Laplace domain as

$$s\overline{C}(\xi, s) + U\frac{\partial \overline{C}}{\partial \xi}(\xi, s) - D\frac{\partial^2 \overline{C}}{\partial \xi^2}(\xi, s) = 0 \tag{16}$$

where $\overline{C}$ is the throat concentration in Laplace space and s is the Laplace variable. The latter equation is subject to the following boundary conditions

$$\overline{C}(0, s) = \overline{C_{\xi_1}}(s) \tag{17}$$
$$\overline{C}(l, s) = \overline{C_{\xi_2}}(s) \tag{18}$$

Equation 16 is a second-order linear partial differential equation whose characteristic polynomial is

$$s + Ur(s) - Dr^2(s) = 0 \tag{19}$$

and whose roots are interpreted as inverse local characteristic lengths

$$r_1(s) = \frac{U + \sqrt{U^2 + 4Ds}}{2D} = \frac{U}{2D} + \delta(s) \tag{20a}$$
$$r_2(s) = \frac{U - \sqrt{U^2 + 4Ds}}{2D} = \frac{U}{2D} - \delta(s) \tag{20b}$$
$$\delta(s) = \frac{\sqrt{U^2 + 4Ds}}{2D} \tag{20c}$$

Hence, general solutions to this homogeneous equation are given as

$$\overline{C}(\xi, s) = A(s)e^{r_1\xi} + B(s)e^{r_2\xi} \tag{21}$$

where the coefficients $A(s)$, $B(s)$ are determined from equations 17 and 18. By rearranging we obtain

$$A(s) = \frac{\overline{C_{\xi_1}}(s)e^{r_2 l} - \overline{C_{\xi_2}}(s)}{e^{r_2 l} - e^{r_1 l}} \tag{22a}$$
$$B(s) = \frac{\overline{C_{\xi_2}}(s) - \overline{C_{\xi_1}}(s)e^{r_1 l}}{e^{r_2 l} - e^{r_1 l}} \tag{22b}$$

By inserting equations 22a and 22b into equation 21 and rearranging, we can obtain the final expression of the throat concentration in Laplace domain as

$$\overline{C}(\xi, s) = e^{\frac{U\xi}{2D}}\frac{\sinh\left(\delta(l-\xi)\right)}{\sinh\left(\delta l\right)}\overline{C_{\xi_1}}(s) + e^{\frac{-U(l-\xi)}{2D}}\frac{\sinh\left(\delta\xi\right)}{\sinh\left(\delta l\right)}\overline{C_{\xi_2}}(s) \tag{23}$$

Notice that equations 21, 22a, and 22b are similar to those introduced by de Arcangelis et al. (1986) and Alvarado et al. (1997) to upscale the longitudinal dispersion in porous media with pore network modeling. Despite the elegant formulation of the Laplace transform technique and its usefulness to perform moment analysis, time-dependent predictions by this method are unlikely limiting its application in practice. Indeed, this technique was classified as distinct from Eulerian mass balance models. In the following subsection we alleviate this limitation by further analytical inversion of equation 23 back into the time domain.

3.2.2 Total solute mass flux in throats

From equation 23 it is straightforward to express the total mass flux of solute concentration $\overline{J} = U\overline{C} - D\frac{\partial \overline{C}}{\partial \xi}$, in Laplace space, at any abscissa, ξ, along the throat

$$\begin{aligned}\overline{J}(\xi, s) = &\frac{e^{\frac{U\xi}{2D}}}{\sinh(\delta(s)l)} \left(\frac{U}{2} \sinh(\delta(s)(l-\xi)) + D\delta(s)\cosh(\delta(s)(l-\xi)) \right) \overline{C}_{\xi_1}(s) \\ &+ \frac{e^{-\frac{U(l-\xi)}{2D}}}{\sinh(\delta(s)l)} \left(\frac{U}{2} \sinh(\delta(s)\xi) - D\delta(s)\cosh(\delta(s)\xi) \right) \overline{C}_{\xi_2}(s)\end{aligned} \tag{24}$$

Then it becomes easier to analytically calculate upstream and downstream total mass fluxes in any throat. These two analytical expressions are given by the following expressions

$$\overline{J}(0, s) = \left(\frac{U}{2} + D\delta(s)\coth(\delta(s)l) \right) \overline{C}_{\xi_1}(s) - De^{-\frac{Ul}{2D}} \frac{\delta(s)}{\sinh(\delta(s)l)} \overline{C}_{\xi_2}(s) \tag{25}$$

$$\overline{J}(l, s) = De^{\frac{Ul}{2D}} \frac{\delta(s)}{\sinh(\delta(s)l)} \overline{C}_{\xi_1}(s) + \left(\frac{U}{2} - D\delta(s)\coth(\delta(s)l) \right) \overline{C}_{\xi_2}(s) \tag{26}$$

3.2.3 Solute concentration in pores

Laplace transform of the mass balance equation 11 at pore i is given as follows

$$V_i s\overline{C_i}(s) = \sum_{l^+} \overline{J_l^+}(\sigma, s)\Gamma_l^+ - \sum_{l^-} \overline{J_l^-}(\sigma, s)\Gamma_l^- \tag{27}$$

which is equivalent to

$$V_i s\overline{C_i}(s) = \sum_{l^+} \overline{J_l^+}(l, s)S_l(l) - \sum_{l^-} \overline{J_l^-}(l, s)S_l(0) \tag{28}$$

where $S_l(\xi)$ is the cross-section area at ξ. Additionally, due to the fluid incompressibility the following expression holds at any pore

$$\sum_{l^+} U_l S_l(l) = \sum_{l^-} U_l S_l(0) \tag{29}$$

Substitution of equations 25, 26, and 29 into equation 28 gives the final expression of the mass balance equations in the pores with respect to Laplace domain

$$\begin{aligned}V_i s\overline{C_i}(s) = &\sum_{j^+} D_{ij} e^{\frac{Pe_{ij}}{2}} a_{ij}(s) S_{ij}(l_{ij})\overline{C}_j(s) + \sum_{j^-} D_{ij} e^{-\frac{Pe_{ij}}{2}} a_{ij}(s) S_{ij}(0)\overline{C}_j(s) \\ &- \sum_{j} D_{ij} a_{ij}(s)\cosh(\delta_{ij}(s)l_{ij}) S_{ij}\overline{C}_i(s)\end{aligned} \tag{30}$$

where $Pe_{ij} = \frac{U_{ij}l_{ij}}{D_{ij}}$ is the Péclet number of throat ij, $a_{ij}(s) = \frac{\delta_{ij}(s)}{\sinh(\delta_{ij}(s)l_{ij})}$ and $\delta_{ij}(s) = \frac{\sqrt{U_{ij}^2 + 4D_{ij}s}}{2D_{ij}}$.

Equation 30 is only valid for internal pores of the network. For other pores, close to upstream or downstream fixed pressure boundaries, a fixed advective mass flux or Neumann second-type boundary condition are typically prescribed. Therefore, equation 30 is slightly modified to account for such boundary conditions.

3.3 Solute Transport Solutions in the Time Domain

The Laplace transformed equations 23, and 30 are analytically inverted back into the time domain. By using complex inversion analysis based on the methods of the contour integration theory, we obtain time-dependent expressions of solute concentrations in pores and throats of the network. In this work, we have avoided to use numerical inverse Laplace transform techniques which are well-known to behave as ill-conditioned problems. Indeed, there is no universal method which is known to work satisfactorily well for all the range of Péclet numbers (Wang & Zhan, 2015). Therefore, in a network where the local Péclet numbers distribution is expected to closely follow the heterogeneity of the local velocity distribution, numerical inversion techniques are not suitable nor stable. More specifically, it was reported (Alvarado et al., 1997) that the numerical Laplace inversion, by the Stehfest method (Stehfest, 1970), was prohibitive for networks larger than 20 x 20 pores and inaccurate for Péclet numbers larger than 10.

By considering s as a complex variable, the Laplace inversion formula is given as follows

$$f(t) = \mathscr{L}^{-1}(\bar{f}(s)) = \lim_{y\to+\infty} \frac{1}{2\pi \mathrm{i}} \int_{x-\mathrm{i}y}^{x+\mathrm{i}y} e^{st} \bar{f}(s)\, ds \tag{31}$$

where $\mathrm{i} = \sqrt{-1}$, $x = \Re(s)$ is an arbitrary real value greater than the real parts of all singularities of $\bar{f}(s)$, and $y = \Im(s)$. The Bromwich integral in equation 31 is evaluated by genuine application of Cauchy's residues Theorem. The resulting functions are not among those lying out in standard tabulated formulas of the inverse Laplace transform. Thus, we use Laurent's series expansion technique for analytical calculation of the residues as fully detailed in Appendices A and B.

3.3.1 Solute concentration in pores

Inverse Laplace transform of equation 30 leads to the following expression (see proof details in Appendix A) for all internal pores

$$\begin{aligned} V_i C_i(t) = &\sum_{j^+} e^{\frac{Pe_{ij}}{2}} S_{ij}(l) \left(K^I_{ij} * C_j\right)(t) + \sum_{j^-} e^{-\frac{Pe_{ij}}{2}} S_{ij}(0) \left(K^I_{ij} * C_j\right)(t) \\ &- \left(\tilde{K}^{II}_i * C_i\right)(t) \end{aligned} \tag{32}$$

where $*$ denotes the convolution product. The throat kernel functions K^I_{ij} and K^{II}_{ij} are given by equations A-24a and A-24b, respectively. The first terms in their expressions are time-independent while the infinite series terms correspond to decaying transient frequencies. The surface-area weighted kernel function $\tilde{K}^{II}_i$ depends only on K^{II}_{ij} as shown in equation A-25. These functions encode Péclet-dependent network modes describing solute transport dynamics of fluid migration in the heterogeneous pore space. Notably, this newly derived formulation is in sharp contrast to the earlier static Eulerian mass balance network approaches such as the mixed-cell methods. Mass balance network modeling by equation 32 explicitly reflects that solute transport at the pore-scale is inherently a nonlocal phenomena whereby the concentration of a pore at present time depends on the concentration history at all pore neighbors. This is equivalent to the semi-empirical approach introduced by Mehmani and Balhoff (2015a). However, the model in equation 32 is more explicit.

3.3.2 Solute concentration in throats

Inverse Laplace transform of equation 23 leads to the following expression for the concentration profile inside a throat (See proof details in Appendix B)

$$C(\xi, t) = K^I_l(\xi, t) * C_{\xi_1}(t) + K^{II}_l(\xi, t) * C_{\xi_2}(t) \tag{33}$$

Where the space- and time-dependent kernel functions K^I_l and K^{II}_l are given by equations B-12a and B-12b, respectively. Equation 33 shows that the concentration profile in a throat depends only on the concentration history of the two pores to which it is attached. The kernel functions provide the time-dependent weights for each concentration value. These kernel functions are expressed as infinite series with decaying time-dependent terms. Equation 33 is optionally applied in a post-processing step after solving for the poral concentrations according to equation 32 to retrieve solute concentration profiles along any desired throat.

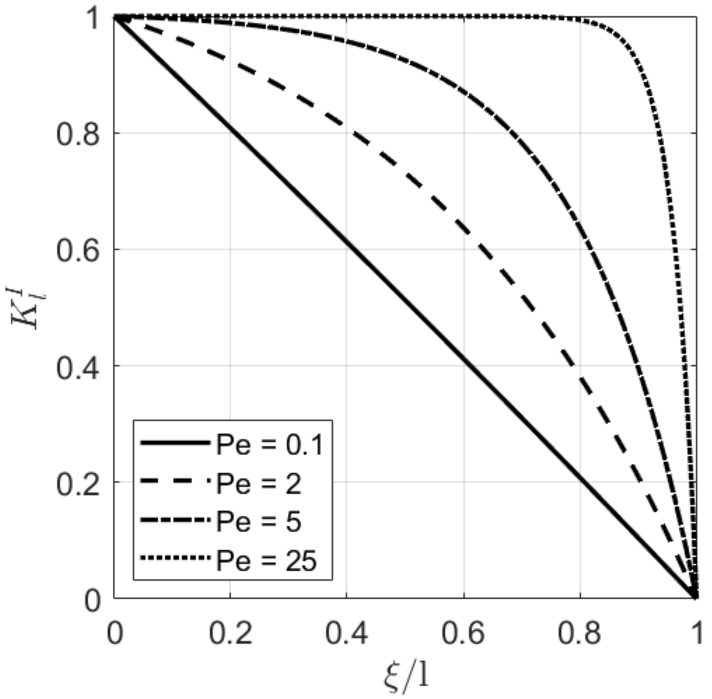

Figure 3. Shape of the asymptotic basis function $K_l^I(\xi/l)$ for different Péclet numbers. Linear weighting of neighbor pore concentrations is only valid when $Pe \rightarrow 0$. For high Péclet numbers the contribution from the upstream pore concentration dominates over a large portion of the channel.

The asymptotic concentration in a throat is obtained from equation D-5 in which $\hat{K}_l^I$ is interpreted as a time-independent weighting basis function. It depends only on the local Péclet number expressing the respective contributions from upstream and downstream pores. Figure 3 plots $\hat{K}_l^I(\xi/l)$ for Péclet numbers 0.1, 2, 5, and 25. A linear behavior results for the smallest Péclet numbers leading to conclude that, in this case, a throat acts as a perfect solute mixer. However, as the Péclet number increases the basis function becomes more concave leading to stronger contribution from the upstream pore concentration and less solute mixing inside the pore channel. Therefore, assuming a simple linear concentration profile in a throat is only accurate under two conditions. The first being the occurrence of an asymptotic regime and secondly only at relatively small Péclet numbers. The results in Figure 3 have been equally obtained by Sadeghi et al. (2020) when developing the exponential scheme considering an exact solution of the steady-state one-dimensional advection-diffusion equation inside a cylindrical throat.

3.4 Comparison to Standard Network Modeling Approaches

This section objective is to investigate the validity range of the various MCM approaches and to identify their formal link with the introduced theory denoted thereafter by the Generalized Mixed-Cell Method (GMCM) and given in equation 32.

The MCM formulations traditionally used to solve for concentration evolution in a pore network are described by the following equation

$$V_i \frac{dC_i}{dt} = \sum_{j^+} U_{ij} S(l) C_j + \sum_{j^-} U_{ij} S(0) C_x + \sum_j D_{ij} S_{ij} \frac{C_j - C_i}{l_{ij}} \tag{34}$$

Equation 34 is a discrete ordinary differential form of equation 10 governing solute transport on nodal pore network positions. The standard MCM scheme results when $C_x = C_i$. This is similar to a first-order upwind finite difference scheme applied to the advective term in continuum scale solute transport modeling (Zheng & Bennett, 2002). The second-order central difference MCM (CD-MCM) scheme results when $C_x = C_j$. This is equivalent to adding the advective term as a correction to the diffusive flux (Sadeghi et al., 2020). The CD-MCM scheme is only stable when $Pe < 2$ whereas the MCM scheme is unconditionally stable.

At a first glance, we will compare the two MCM formulations with the asymptotic form of equation 32 given by the following equation (See Appendix C for a complete derivation) and denoted by GMCM$_\infty$ thereafter. The GMCM$_\infty$ is obtained while the diffusion time t_{diff} is going to zero keeping the Péclet number Pe constant.

$$\begin{aligned} V_i \frac{dC_i}{dt} = & \sum_{j^+} U S(l) \frac{e^{\frac{Pe}{2}}}{2\sinh\left(\frac{Pe}{2}\right)} C_j + \sum_{j^-} U S(0) \frac{e^{\frac{-Pe}{2}}}{2\sinh\left(\frac{Pe}{2}\right)} C_j \\ & - \sum_j \frac{1}{2} U S \coth\left(\frac{Pe}{2}\right) C_i \end{aligned} \tag{35}$$

Equation 35 is still markedly different from equation 34. The GMCM$_\infty$ formulation has an explicit (and inherited) dependence on local Péclet numbers indicating that MCM formulations might be valid for a limited range of Péclet regimes. The later intuition leads to investigate the asymptotic behavior of the GMCM$_\infty$ formulation for advective and diffusive dominant regimes, respectively. Proofs given in Appendix C are instrumental to show that the CD-MCM and standard MCM schemes are particular cases of the GMCM$_\infty$ formulation for the lowest and highest Péclet regimes, respectively.

These theoretical findings shed light on the limitations of the MCM formulations as general-purpose modeling techniques for transport in pore networks. Their validity range is limited to strongly dominant advective and diffusive regimes. This is in agreement with the numerical experiments by Sadeghi et al. (2020) showing that MCM is not an accurate method even at steady-state. Indeed, the local distribution of Péclet numbers inside a 3D disordered network may span several orders of magnitude as shown in Figure 4. Hence, the MCM validity range will be exceeded for an important number of sites.

3.5 Numerical Solution Scheme

The resulting sparse linear system of equations 5 has a symmetric and positive-definite global conductance sparse matrix. It is solved with standard sparse direct or iterative solvers such as multifrontal techniques (Davis, 2004) or the preconditioned conjugate gradient methods (Saad, 2003), respectively. Direct methods outperform iterative methods for network size less than $n_p \approx 10^4$ pores. For very large networks, iterative methods are accelerated with algebraic multigrid preconditioning techniques.

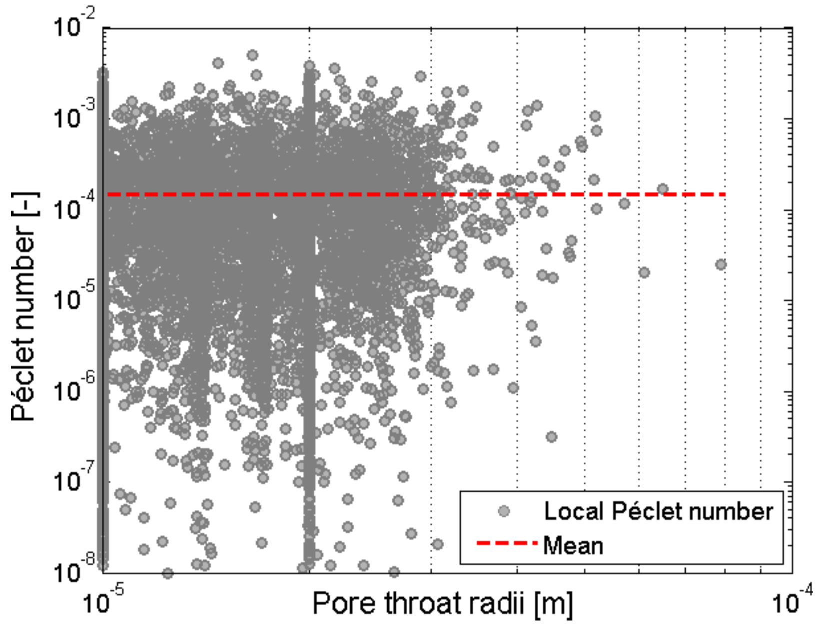

Figure 4. Distribution of the local Péclet numbers versus throat radii's inside the Berea sandstone pore network model from Øren and Bakke (2003).

In this subsection, we give the final expressions of the linear equations systems resulting from space-time discretization of the solute transport equations 32 in a pore network. Next, we show how to use the particular features of the convolution kernels to gain in computational efficiency through development of an accelerated numerical scheme.

We discretize the poral system of equations 32 in the time domain by the Crank-Nicolson algorithm. The final form of the linear equations system at time step m is given as follows

$$[A]^m\{C\}^m = \sum_{k=1}^{m-1}[A]^k\{C\}^k + \{F\}^m \tag{36}$$

where $[A]^k(0 < k < m)$ matrices are contributions from the tracer concentration history in the network. These matrices entries are analytically computed from the formulas of the convolution kernels. The last term in equation 36 corresponds to the vector $\{F\}^m$ holding the contribution from boundary conditions.

Notice that entries of the k^{th} adjacency matrix $[A]^k$ are computed analytically and may be interpreted as weights to previously computed concentration distributions in the network at time step k. This numerical formulation retains therefore several levels of implicitness into the numerical scheme owing to the dynamic behavior of the generalized mass balance formulation. By keeping all these memorised dynamics we expect to compute a more accurate concentration field. However, this is accomplished with lower computational efficiency and an increase of computer memory storage. To remedy to this situation, we make use of observations from porous media physics. The latter dictates that an optimal threshold, m_τ, for the number of terms, m, to keep in equations 36 depends on the distribution of local Péclet numbers and the network shapes distributions. For instance, within a pore network with uniform shape properties we expect m_τ to increase as Pe decreases. The objective of this section is to develop a theoretical criterion which estimates m_τ to keep a good balance between required numerical solution accuracy and the computational effort.

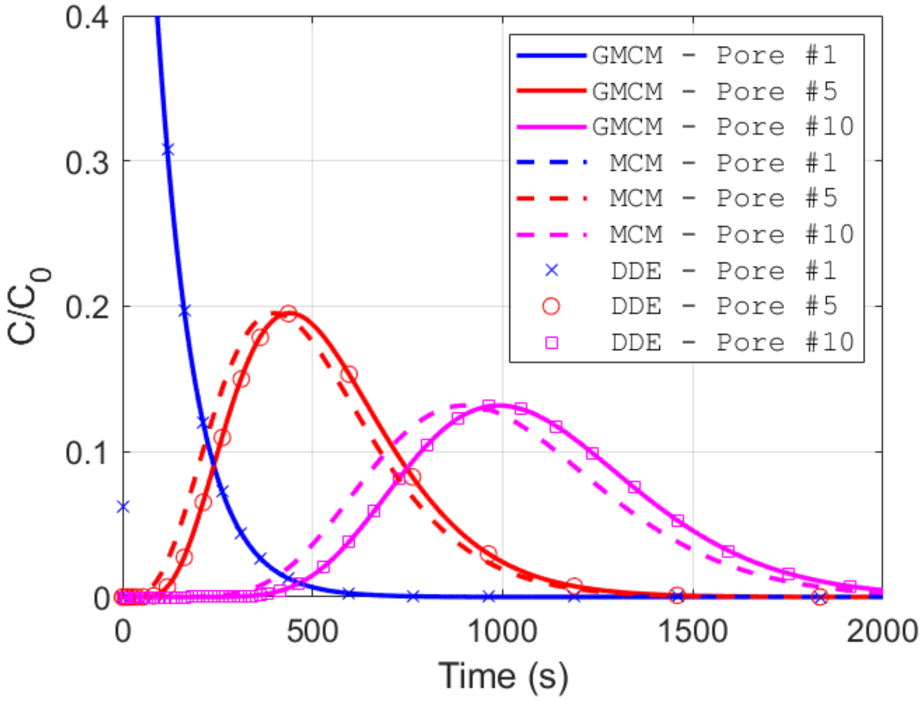

Figure 5. Comparison between the generalized mixed-cell method (GMCM), the mixed-cell method (MCM), and the delay differential equations (DDE) approaches for modeling purely advective solute transport evolution in a one-dimensional pore network model with uniform geometrical properties. Computed concentrations by the MCM breakthrough earlier owing to neglecting solute transport in throats. The GMCM and DDE simulation results are in excellent agreement demonstrating the equivalence of these two formulations for a purely advective transport regime.

We use the special properties of the convolution kernels, K_{ij}^{I} and K_{ij}^{II}, involved in the discrete transport model to accelerate the computational work. By denoting the relative error between the first term and the sum of the time-dependent terms in these series as ε, we can define for each convolution kernel function a characteristic time, τ_l, at which it can be considered as constant and all time-dependent terms becomes negligible. This characteristic time is approximated by the following formula

$$\tau_l = max\left[-\frac{l^2}{D(\pi^2+\frac{Pe^2}{4})}ln\left(\frac{\varepsilon Pe\left(\pi^2+\frac{Pe^2}{4}\right)}{4\pi^2}\coth\left(\frac{Pe}{2}\right)\right),0\right] \tag{37}$$

τ_l is simply interpreted as the time at which the solute transport asymptotic regime is reached at throat l. Hence, for times higher than $\tau = \max_l(\tau_l)$ the solute transport in the whole network reaches an asymptotic regime. τ depends solely on local characteristic diffusion times, $t_{diff} = \frac{l^2}{D}$, and local Péclet numbers. Equation 37 shows that, τ is the global maxima of the function $\phi(t_{diff}, t_{adv}) = t_{diff} f^{\varepsilon}(Pe)$ where t_{adv} is a characteristic advection time. The function $f^{\varepsilon}(Pe)$ is expressed as

$$f^{\varepsilon}(Pe) = max\left[-\frac{1}{\left(\pi^2+\frac{Pe^2}{4}\right)}ln\left(\frac{\varepsilon Pe\left(\pi^2+\frac{Pe^2}{4}\right)}{4\pi^2}\coth\left(\frac{Pe}{2}\right)\right),0\right] \tag{38}$$

We note first that t_{diff} determines the magnitude of τ according to a linearly increasing relationship. Then, for a fixed t_{diff}, τ decreases as Pe increases. The above analysis leads to a simplified calculation of $[A]^k (0 < k < m)$ matrices involved in the numerical solution of pore concentrations at time t_m, which are calculated from convolution kernels over time intervals $[t_m - t_{k+1}, t_m - t_k]$ and $[t_m - t_k, t_m - t_{k-1}]$. Indeed from the relaxation time τ, we are able to set the integer $k_\tau^m = max\{k \in [1, m] \mid t_m - t_k \geq \tau\}$ that determines the time at which the asymptotic regime is reached in the network. It follows that the matrices $[A]^k (0 < k < k_\tau^m)$ are equal to a constant $[A]_\infty$ adjacency matrix corresponding to the asymptotic regime. These findings allow us to define the integer $m_\tau = m - k_\tau^m$ and the vector $\{Q\}^m = \sum_{k=1}^{m-m_\tau-1} [A]_\infty \{C\}^k$ for $m > m_\tau$ such that the numerical scheme given in the equations system 36 becomes

$$[A]^m \{C\}^m = \sum_{k=1}^{m-m_\tau-1} [A]^k \{C\}^k + \{F\}^m \quad \text{for} \quad m \leq m_\tau \tag{39a}$$

$$\begin{cases} [A]^m \{C\}^m & = \sum_{k=m-m_\tau}^{m-1} [A]^k \{C\}^k + \{Q\}^m + \{F\}^m \\ \{Q\}^m & = \{Q\}^{m-1} + [A]_\infty \{C\}^{m-m_\tau} \end{cases} \quad \text{for} \quad m > m_\tau \tag{39b}$$

Note that m_τ is bounded between $\lfloor \frac{\tau}{dt_{min}} \rfloor$ and $\lfloor \frac{\tau}{dt_{max}} \rfloor$ where dt_{min} and dt_{max} are the minimum and maximum allowed time steps, respectively. Therefore, the resulting numerical scheme satisfies that the maximum number of $[A]^k$ matrices calculations is determined a priori by m_τ which is a bounded integer. Therefore, this scheme is expected to effectively reduce the computational burden needed to solve solute transport equations in a pore network. This will be addressed in the following.

4 Results and Discussions

4.1 One-Dimensional Pore Network Verification Problem

Consider a one-dimensional network where all its n_p pores are serially linked with $n_p - 1$ throats. We assume that all pores and throats have a uniform volume V, length l and cross-section area S, respectively. We further assume a purely advective mode of solute transport with a uniform centerline velocity u along the throats. For this problem, the pores behave as reservoirs whose solute filling and drainage depends solely on the geometrical properties of the network. According to the delay differential equations (DDE) approach applied to a pore network (Martins et al., 2009), this problem is governed by the following system

$$\frac{dC_1}{dt} = C_0 - q_1^- C_1(t) \tag{40a}$$

$$\frac{dC_n}{dt} = q_n^+ C_{n-1}(t - \tau) - q_n^- C_n(t) \quad for \quad 1 < n \leq n_p \tag{40b}$$

where C_n is the concentration at the n^{th} pore, C_0 is an inlet pulse concentration entering the first pore at $t = 0$, $\tau = l/u$ is the time lag induced by solute transport in the upstream channel, while q_n^+ and q_n^- are the upstream/downstream specific pore filling/drainage frequency, respectively. Because channels cross-sections and pore volumes are uniform, $q = q_n^+ = q_n^- = \frac{uS}{V}\ \forall\ n$ for this particular situation. Equations 40a-40b are identical to the MCM formulation given in equation 34, except that the diffusive term is neglected and the upstream advective term is delayed with a constant. In general, the delay magnitude τ would be different at each pore when the throats length distribution is non-uniform. Hence, τ figuring in equation 40b would be replaced by τ_{n-1}.

Equations 40a-40b admit the following analytical solution

$$C_n(t) = H(t_{n,\tau}) \frac{(q t_{n,\tau})^n e^{-q t_{n,\tau}}}{n!} C_0 \tag{41}$$

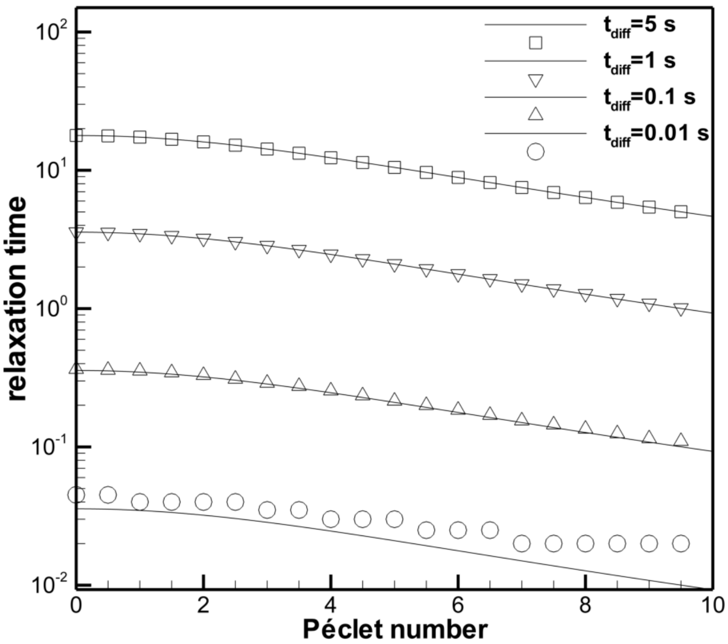

Figure 6. Evolution of the relaxation time, τ, with the local Péclet number inside a throat for a given characteristic diffusion time, $t_{diff} = \frac{l^2}{D}$. Symbols show the numerically calculated values while solid lines represent the analytical calculations by equation 37.

where H is the Heaviside function and $t_{n,\tau} = t - (n-1)\tau$. Equation 41 is useful for basic verification of solute transport modeling with pore network models which is reported herein for the first time to our best knowledge. This will ensure that model equations were correctly implemented. Equation 41 could be alternatively obtained by simplifying equation 32 for this particular problem. A demonstration was given by Kamtchueng (2016) and will not be repeated herein. The introduced model accuracy was favorably checked with the analytical solution provided in equation 41 (Kamtchueng, 2016) demonstrating that the model was correctly implemented. Furthermore, here we perform a three way comparison involving the newly introduced formulation, the legacy mixed-cell method and a numerical solution of the so-called delay differential equations approach. For the latter, the MATLAB function *dde23* was used for numerical integration. This is a specialized solver for DDEs with constant delays featuring an explicit Runge-Kutta triple scheme (Dormand & Prince, 1986; Shampine & Thompson, 2001). Figure 5 shows the results of this inter-comparison study for a network with $n_p = 10$ at positions strategically selected at the entry, middle and the outlet of the one-dimensional network. Additional model parameters are $V = 10^{-14}$ m^3, $l = 10^{-4}$ m, $S = 10^{-11}$ m^2 and $u = 10^{-5}$ $m^2 s^{-1}$. Thus, $q = 10^{-2}$ s^{-1} and $\tau = 10$ s. Except for the first pore where the concentration decays rapidly, asymmetric bell shaped curves characterize the concentration history in other pores. As expected, solute dispersion increases and the maximal concentration decreases as the distance separating the pore from the source increases. Concentrations computed by the DDE and GMCM approaches are in excellent agreement. This provides an additional model validation of the GMCM approach. Furthermore, it provides an evidence that solute transport breakthrough earlier when relying on the MCM approach because solute transport in throats is neglected. This is concluded from figure 5 when comparing the MCM concentration histories to those computed with other approaches. Mass conservation was checked by calculating the mass under the concentration history curves (i.e. $M_0 = \int_0^\infty C_n(t)dt$) for all pores. The largest GMCM deviation from the analytical value does not exceed 1.3 10^{-3} at the last pore. Moreover, theoretical analysis (Kamtchueng, 2016) have shown that the maximal concentrations, C_n^{max}, scale with $t^{-1/2}$. The first-order analytical moment giving the time at which C_n^{max} is attained is $t_n^{max} = \frac{n}{q} + (n-1)\tau$. The second-order moment can also be analytically determined as $M_{n,2} = \frac{(n-1)^2q^2\tau^2+2(n-1)nq\tau+n(n+1)}{q^2}$.

Assessment of the aforementioned acceleration process efficiency is evaluated according to a priori determination of the system characteristic relaxation time, the central processing unit (CPU) time, and the numerical solution accuracy. The relaxation time of the porous medium is the maximal value of all local relawation times. Hence, a simple evaluation of equation 37 would be sufficient. Here, we compare this analytical calculation of the relaxation time with its numerical counterpart deduced from the characteristics of the convolution kernels. Figure 6 shows the evolution of analytical and numerical relaxation times versus the local P*é*clet number for different diffusion times, t_{diff}. There is an excellent match between the two solutions meaning that equation 37 can accurately predict the relaxation time.

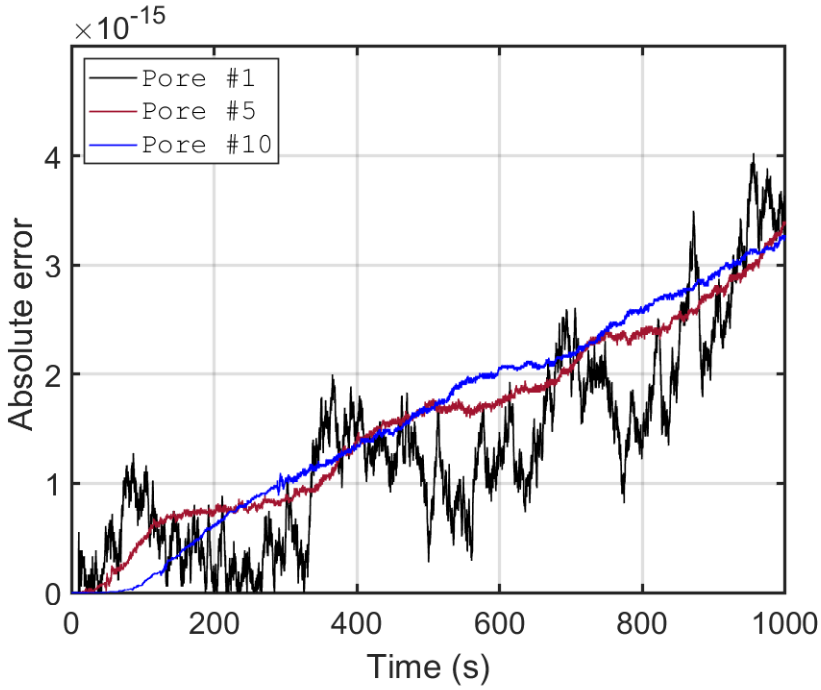

Figure 7. Time-dependent numerical error of simulated concentrations in some pores of the one-dimensional network. This is the net difference between simulated values by the full and optimized numerical schemes given by equations 36 and 39a-39b, respectively.

Many solute transport simulations spanning a total time of $1,000$ s were processed for different values of, m_τ, in equations 39a and 39b. A uniform time step size equal to 0.1 s was used. Table 1 indicates that for decreasing values of m_τ the CPU time drops dramatically. Indeed, the speedup exceeds $1,500$ when $m_\tau = 1$. The accuracy of the accelerated numerical scheme is shown on Figure 7 which depicts, for some selected pores, the time dependent absolute error between the full and optimal numerical schemes given in equations 36 and 39a-39b, respectively. Chosen problem parameters imply that the relaxation time of the system equals $\tau = 3.57\ 10^{-2}$ s, hence $m_\tau = 2$. Figure 7 indicates that the numerical error of the accelerated scheme is in the range of floating point arithmetic round-off error.

Table 1. CPU time (s) and speedup factor of solute transport simulations with the pore network model for the one-dimensional test problem as m_τ decreases.

m_τ	CPU time (s)	Speedup factor
10^4	48,615	1
10^2	1,052	46
50	512	95
10	123	395
1	31	1,568

Observed efficiency and accuracy of the optimal numerical scheme are expected to scale for complex disordered three-dimensional pore networks provided that m_τ is properly chosen.

4.2 Application to a 3D Pore Network Model

The sandstone at Berea, in Ohio, is an oil and gas bearing formation composed from major amounts of silicates (more than 90 % of Quartz) and minor proportions of feldspars and carbonates. Therefore, we assume minor reactivity of the injected aqueous solution with the host rock effectively reducing the problem into a single component tracer. This sandstone is widely used for core analysis and flooding experiments due to its fine grained texture, and well-sorted characteristics (Dullien, 1992). We use herein the pore network of Berea sandstone from Øren and Bakke (2002, 2003) shown in Figure 8, and which has been extensively used in the literature to predict single and multiphase transport properties (Valvatne et al., 2002; Piri & Blunt, 2005b, 2005a). This classic pore network is extracted from a process based image reconstruction using Voronoï tessellation techniques. Øren and Bakke (2002, 2003) were able to reconstruct 3D sandstone images from available information in two-dimensional thin cross-section images. Geological processes such as deposition, diagenesis, were emulated to generate an equivalent digital rock which was successfully compared with experimental Berea microstructure. Main features such as coordination number, pore and throat size distributions were captured by this technique. This reconstructed digital rock was transformed into a topologically equivalent network that was proposed as a benchmark test case for pore-scale network modeling. The reconstructed three-dimensional image is a cube with 3 mm edge length along each space direction, leading to a total rock volume of 27 mm^3. It has a net porosity of 18.3 % and a calculated permeability of 2668 mD. The extracted network has a total of $38,495$ elements divided into $12,349$ pores and $26,146$ throats as illustrated in Figure 8. This Figure shows also the shape factor distributions for the network elements. The average inscribed radius is 19.17 μm for pores and 10.87 μm for throats. Figure 8 shows the distributions of network elements radii's. The average coordination number is 4.19 while its maxima equals 19.

We simulate the injection of a unit concentration pulse aqueous solution at the inlet boundary of the network. The concentration field is monitored inside the extracted pore network model when using the GMCM formulation (Equations 39a-39b) and its asymptotic form (Equation 35). Computed Log_{10} scale concentration fields at selected times are shown in Figure 9. At early times, we clearly notice the solute local dispersion and the gradual attenuation of the solute maximal concentration. At later times, we notice the tendency of the concentration field to stabilise as steady-state is approached. In the GMCM_∞ simulation the same input parameters were used. The computation simply excluded all transient terms inside the infinite series in the convolution kernels. As MCM are special cases of GMCM_∞ this last model will give a more

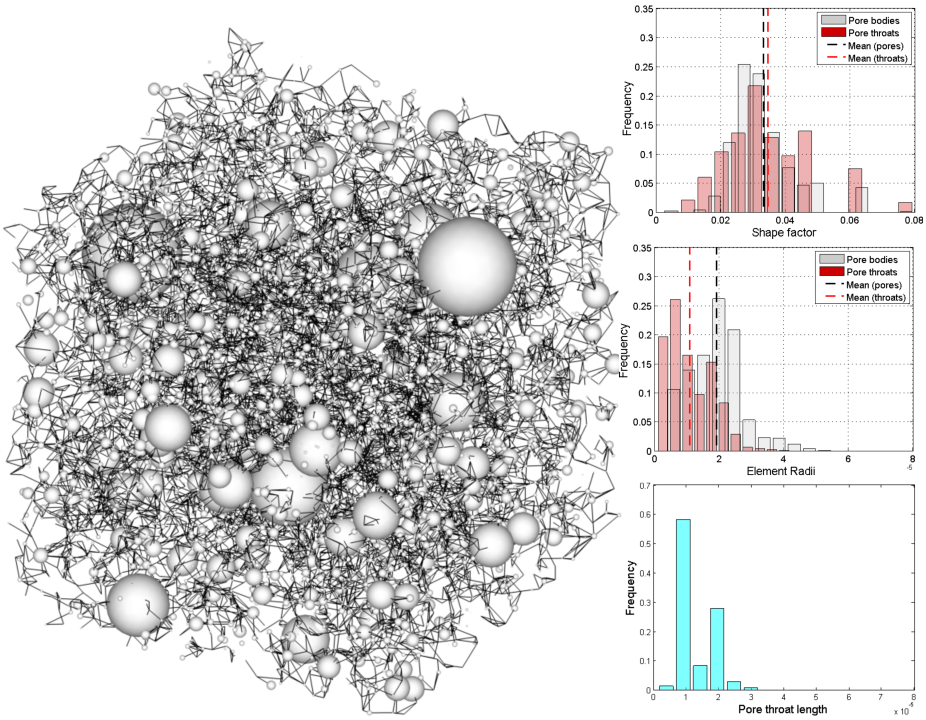

Figure 8. Pore network model of the Berea sandstone from Øren and Bakke (2003). Sphere size is proportional to pore volume and does not represent this element shape. Solid lines represent the throats.

accurate answer of all static models. Results of the comparison between the dynamic and the asymptotic transport models are presented as distributions of percent relative concentration error given as follows

$$Err_i = 100\left(1 - \frac{C_i^{GMCM_\infty}}{C_i^{GMCM}}\right) \tag{42}$$

where $C_i^{GMCM_\infty}$ and C_i^{GMCM} are the corresponding pore concentrations, respectively.

Figure 10-a shows the relative concentration error distribution at 60 s. This error exceeds the thresholds of 10 % and 20 % at 66.5 % and 31.9 % of the porous media space, respectively. Figure 10-b shows similar results at 120 s, but with an error distribution more concentrated on the left. Hence, the error in 91.5 % of the pores exceeds 10 %. This error attenuates only to the limit of a steady-state concentration regime. Hence, the asymptotic GMCM$_\infty$ (and consequently the MCM) approaches are inaccurate for pore-scale mass transport network modeling. The introduced GMCM model is a more accurate alternative which can be used for general-purpose applications. The magnitude of the relative error distribution is expected to grow significantly in the occurrence of nonlinear mass transport processes. For instance, owing to the logarithmic nature of the mass action law for thermodynamically controlled reactive aqueous species, the error will grow with several orders of magnitude for the secondary aqueous species. This can potentially drive mineral dissolution and precipitation reactions along a different, or even a reversed, pathway. This is expected to occur for moderate to slow kinetically controlled reactions as the time required to reach an equilibrium state would be very long. Therefore, earlier reactive transport models based on static network approaches, such as the MCM, are far from being predictive as already men-

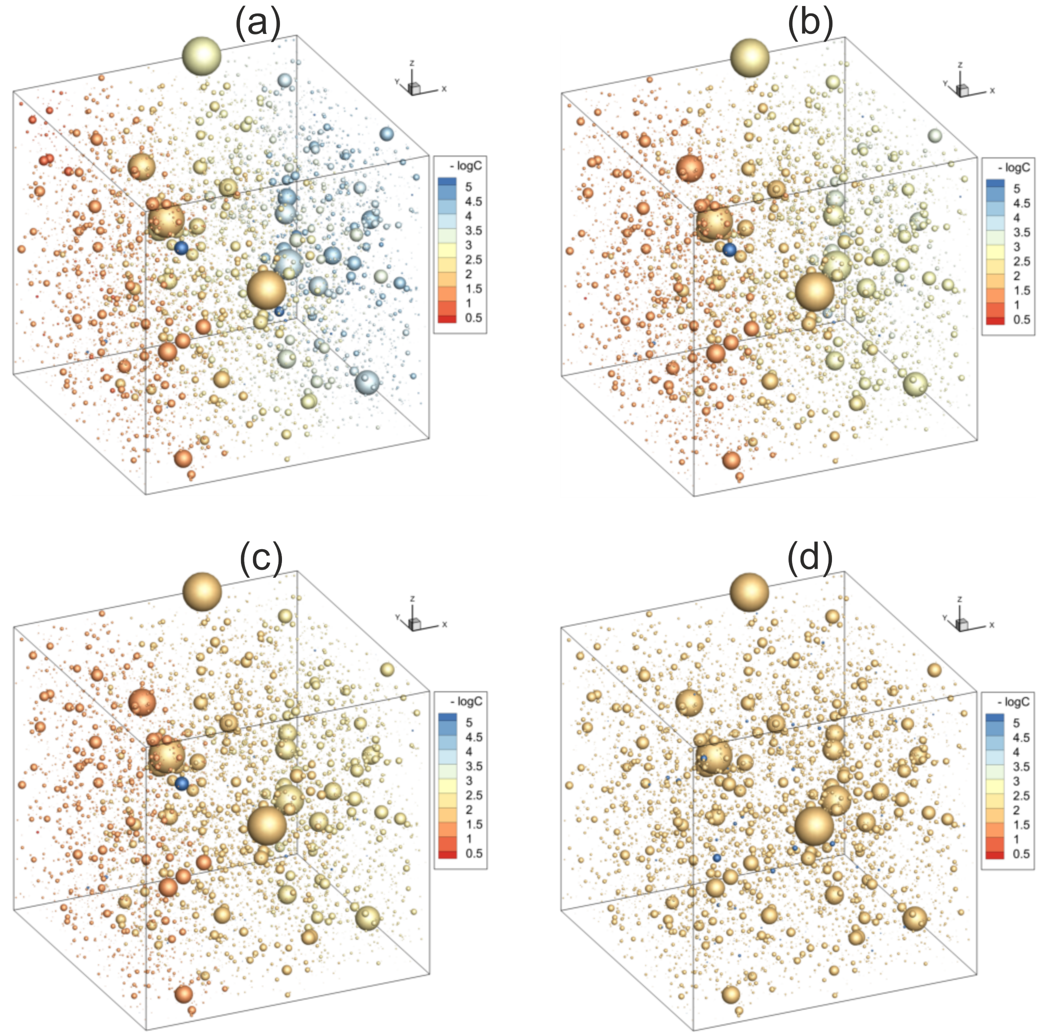

Figure 9. Results of the solute transport simulation in Berea network model with the generalized mixed-cell mass balance formulation. A unit pulse is injected at the inlet flow boundary. Computed concentrations fields in Log_{10} scale units are visualized at (a) 30, (b) 60, (c) 120, and (d) 300 seconds.

tioned by several authors (Acharya et al., 2005; L. Li et al., 2006, 2008; Kim et al., 2011; Raoof et al., 2012; Mehmani et al., 2012; Raoof et al., 2013; Tansey & Balhoff, 2016). Additional research efforts towards this challenging endeavor can benefit from the method developed in this paper by deploying the operator splitting techniques (Steefel & MacQuarrie, 1996).

In this work, we markedly make a shift from static network transport models to dynamic models where transitions across the whole range of Péclet regimes are consistent according to sound theoretical foundations. This is an important evolution of pore network modeling of solute transport processes. The developed general-purpose formulation could be easily extended to support local linear solute transport such as equilibrium sorption. Additionally, the assumption of zero initial concentration could be easily relaxed. The developments in this paper adopted this assumption to simplify the presentation. The closed-form analytical solutions give additional insights into the physics of pore-scale solute transport by explicitly showing its dependence on the local

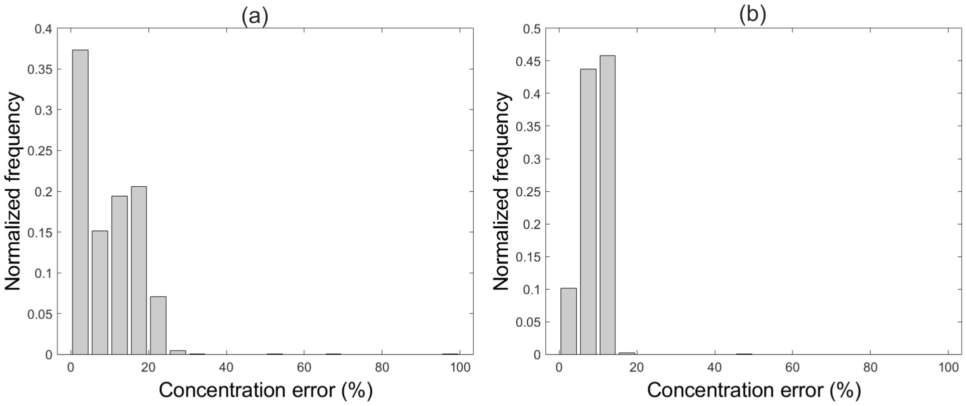

Figure 10. Results of the quantitative comparison between the generalized mixed-cell mass balance and its asymptotic variant. Relative concentration error distributions at (a) 60 and (b) 120 seconds illustrating the unsuitability of the asymptotic mass balance scheme for modeling pore-scale solute transport processes.

Péclet number distribution through time and space dependent convolution kernels. Similar to MCM approaches, the model assumes perfect mixing within pores. Recent works indicate that this has negligible impact on dispersion modeling in disordered pore networks (Mehmani & Balhoff, 2015b; Yang et al., 2016). One-dimensional averaging of the solute transport equation in throats preclude this model to predict the power-law dispersion regime owing to neglecting the shear dispersion effects (Mehmani & Balhoff, 2015a). Future work can focus on borrowing few ideas from the so-called superposing transport method. However, we believe that explicitly including the shear dispersion effects in all network throats to improve the presented formulation in this paper will lead to a highly complex model.

5 Conclusions

Sustained rapid progress of non-invasive three-dimensional porous media instrumentations opens new frontiers to pore-scale modeling. However, compared to recent advances in multiphase fluid flow, there is much less progress targeting network modeling of solute transport processes. The merit of this paper is to bring a rigorous mathematical derivation leading to a general-purpose non-local Eulerian network model. Key findings are summarized as follows:

1. A novel general-purpose mixed-cell formulation is introduced for transport network modeling. The pore solute concentration depends on the concentration history in neighbor pores. Time-dependent and exponentially decaying convolution kernels provide the weights of current and past time contributions from these pores.
2. This formulation can recover, a posteriori, the solute transport profile in any throat by simple post-processing of the numerical solution at its pore-throat-pore assembly.
3. Popular mixed-cell methods are found to be equivalent to the end members of the generalized asymptotic formulation for the advective and diffusive dominant regimes. Hence, the roots of these techniques are identified showing that they form two-level approximates.

4. The numerical scheme is highly optimized making profit from the properties of the convolution kernels preserving the efficiency of the mixed-cell methods for network modeling.
5. The model was favourably compared to a simple analytical solution and the delay differential equations approach. The expected concentrations are reproduced unlike for the mixed cell method characterized by early breakthrough and first-order moment.
6. Testing on the Berea network extracted from a reconstructed three-dimensional digital image confirms the higher accuracy of the generalized approach and the unsuitability of the asymptotic schemes, including our GMCM_∞ scheme, for modeling dispersion on pore networks.

The proposed approach could find many applications in all fields of porous media beyond geosciences related disciplines. This is more likely when interactions at the fluid-solid interfaces lead to retarded migration of solute and heat between all phases in the system.

Acknowledgments

The corresponding author was partially supported by the French Research Agency (ANR) in the Framework of CGS-μLab project. T. Kamtchueng was supported by joint PhD fellowships from BRGM (French Geological Survey) and research funds provided by '*Région Centre Val de Loire*'.

Appendix A Inverse Laplace transform of concentrations in pores

A.1 Regularisation of solute transport equation in Laplace space

Prior analysis (not shown herein) of different terms in the right-hand side of equation 30 allowed us to conclude that some of them diverge as $s \to +\infty$. As such, Jordan's Lemma is not applicable to these functions which precludes direct application of the residues Theorem. To avoid this problem, equation 30 is regularised by dividing it by s^3, such that

$$\begin{aligned} V_i \frac{\overline{C_i}(s)}{s^2} &= \sum_{j^+} D e^{\frac{Pe}{2}} \frac{a(s)}{s^3} S(l) \overline{C_j}(s) + \sum_{j^-} D e^{-\frac{Pe}{2}} \frac{a(s)}{s^3} S(0) \overline{C_j}(s) \\ &- \left[\sum_{j^+} D \frac{a(s)}{s^3} \cosh(\delta l) S(l) + \sum_{j^-} D \frac{a(s)}{s^3} \cosh(\delta l) S(0) \right] \overline{C_i}(s) \end{aligned} \tag{A-1}$$

Notice that throughout this Appendix the ij notation for throat related variables is dropped for simplicity. Let's additionally introduce the following equation

$$\begin{aligned} V_i \overline{C_i}(s) = &\sum_{j^+} D e^{\frac{Pe}{2}} \frac{a(s)}{(s-\varepsilon)} S(l) \overline{C_j}(s) \\ &+ \sum_{j^-} D e^{-\frac{Pe}{2}} \frac{a(s)}{(s-\varepsilon)} S(0) \overline{C_j}(s) \\ &- \sum_{j^+} D \frac{a(s)}{(s-\varepsilon)} \cosh(\delta l) S(l) \overline{C_i}(s) \\ &+ \sum_{j^-} D \frac{a(s)}{(s-\varepsilon)} \cosh(\delta l) S(0) \overline{C_i}(s) \end{aligned} \tag{A-2}$$

Because the inverse Laplace transforms of terms in equation A-1 are equivalent to limits of corresponding second primitive terms in equation A-2 when $\varepsilon \to 0$, we directly work on inversion of equation A-1 into the time domain. Furthermore, owing to the linearity of the inverse Laplace transform operator, $\mathscr{L}^{-1}$, the inversion could be performed independently for each term of this linear algebraic equation.

A.2 Residues calculations

We will use the series method (Schiff, 1999) to determine the poles and residues at the singularities of identified functions. This involves finding Laurent series expansions from which the residue is equivalent to a_{-1} coefficient of the Laurent series. Only two types of functions will be involved in the Laplace inversion process, so we start by calculating the residues at their poles as discussed below.

A.2.1 Residues of $\mathbf{I}(s)$ *term*

Let's consider the terms in equation A-2 taking the following general form

$$\mathrm{I}(s) = D\frac{a(s)}{s-\varepsilon} \tag{A-3}$$

by using the definition of $a(s) = \frac{\delta(s)}{\sinh(\delta(s)l)}$ in combination with Euler's formula for the hyperbolic sine function, we obtain

$$a(s) = \frac{\mathrm{i}\delta(s)}{\sin(\mathrm{i}\delta(s)l)} \tag{A-4}$$

we will further use the partial fraction expansion technique to express the complex sine function as infinite series

$$\frac{\pi}{\sin(\mathrm{i}\delta(s)l)} = \frac{\pi}{\mathrm{i}\delta(s)l} - 2\frac{\mathrm{i}\delta(s)l}{\pi}\sum_{n=1}^{+\infty}\frac{(-1)^n}{n^2+\frac{(\delta(s)l)^2}{\pi^2}} \tag{A-5}$$

Insertion of equations A-4 and A-5 into equation A-3 leads to

$$\mathrm{I}(s) = \frac{D}{(s-\varepsilon)l}\left(1+2\sum_{n=1}^{+\infty}\frac{(-1)^n\,(\delta(s)l)^2}{(n\pi)^2+(\delta(s)l)^2}\right) \tag{A-6}$$

and by noting that

$$\frac{l^2}{D}(s-z_n) = (n\pi)^2 + (\delta(s)l)^2 \tag{A-7}$$

where

$$z_n = -\left(\frac{Dn^2\pi^2}{l^2}+\frac{U^2}{4D}\right) = -\frac{D}{l^2}\left(n^2\pi^2+\frac{Pe^2}{4}\right) \tag{A-8}$$

the residue of $\mathrm{I}(s)e^{st}$ at its n^{th} pole, z_n, is equal to the coefficient of $(s-z_n)^{-1}$ in the series expansion of $\mathrm{I}(s)e^{st}$ around z_n (Schiff, 1999), and because $(\delta(z_n)l)^2 = -(n\pi)^2$ results from direct application of equation A-7 we get

$$Res\left(\mathrm{I}(s)e^{st}, z_n\right) = -\frac{D^2}{(z_n-\varepsilon)l^3}\left(2(-1)^n(n\pi)^2\right)e^{z_n t} \tag{A-9}$$

while the residue of $\mathrm{I}(s)e^{st}$ at ε is simply deduced from its definition

$$Res\left(\mathrm{I}(s)e^{st}, \varepsilon\right) = D\frac{\delta(\varepsilon)}{\sinh(\delta(\varepsilon)l)}e^{\varepsilon t} \tag{A-10}$$

where $\delta(\varepsilon) = \frac{\sqrt{U^2+4D\varepsilon}}{2D}$ comes from direct application of equation 20c.

574 #### *A.2.2 Residues of* $\mathrm{II}(s)$ *term*

Similarly, let's denote terms of type II appearing in equation A-2 by

$$\mathrm{II}(s) = \mathrm{I}(s)\cosh(\delta(s)l) \tag{A-11}$$

by combining equations A-11 and A-6 we obtain the Laurent series expansion of $\mathrm{II}(s)$ as

$$\mathrm{II}(s) = D\frac{\cosh(\delta(s)l)}{(s-\varepsilon)l}\left(1 + 2\sum_{n=1}^{+\infty}\frac{(-1)^n(\delta(s)l)^2}{(n\pi)^2 + (\delta(s)l)^2}\right) \tag{A-12}$$

by analogy to preceding developments and by noting that $\delta(z_n)l = \mathrm{i}n\pi$, we can get the residue of $\mathrm{II}(s)e^{st}$ at pole z_n as

$$Res\left(\mathrm{II}(s)e^{st}, z_n\right) = -\frac{D^2\cosh(\mathrm{i}n\pi)}{(z_n-\varepsilon)l^3}\left(2(-1)^n(n\pi)^2\right)e^{z_nt} \tag{A-13}$$

which simplifies into

$$Res\left(\mathrm{II}(s)e^{st}, z_n\right) = -\frac{2D^2}{(z_n-\varepsilon)l^3}(n\pi)^2e^{z_nt} \tag{A-14}$$

finally, the residue of $\mathrm{II}(s)e^{st}$ at ε is simply

$$Res\left(\mathrm{II}(s)e^{st}, \varepsilon\right) = D\delta(\varepsilon)\coth(\delta(\varepsilon)l)e^{\varepsilon t} \tag{A-15}$$

575 ### A.3 Inverse Laplace expressions of $\mathbf{I}(s)$ and $\mathbf{II}(s)$

In the following we use Cauchy's residue theorem (Schiff, 1999) in conjunction with Jordan's Lemma leading to the following so-called complex inversion formula for a function $\bar{f}(s)$ having infinitely many poles at $\{z_n\}_{n=1}^{\infty}$ where $z_n \to \infty$ as $n \to \infty$

$$\mathscr{L}^{-1}(\bar{f}(s)) = \sum_{n=1}^{+\infty} Res\left(\bar{f}(s)e^{st}, z_n\right) \tag{A-16}$$

where $\bar{f}(s)$ is one of the two functions $\mathrm{I}(s)$ or $\mathrm{II}(s)$ analysed previously. Hence,

$$\begin{aligned}\mathscr{L}^{-1}\left(\mathrm{I}\right)(t) = {} & \lim_{\varepsilon\to 0} D\frac{\delta(\varepsilon)}{\sinh(\delta(\varepsilon)l)}e^{\varepsilon t} \\ & - \frac{2D^2}{l^3}\sum_{n=1}^{+\infty}\frac{(-1)^n(n\pi)^2}{z_n}H(t)e^{z_nt}\end{aligned} \tag{A-17}$$

The first term in the right hand side of equation A-17 could be easily calculated from respective definitions of $\delta(s)$ and Pe as

$$\lim_{\varepsilon\to 0} D\frac{\delta(\varepsilon)}{\sinh(\delta(\varepsilon)l)}e^{\varepsilon t} = \frac{U}{2\sinh\left(\frac{Pe}{2}\right)} \tag{A-18}$$

Similarly,

$$\begin{aligned}\mathscr{L}^{-1}\left(\mathrm{II}\right)(t) = {} & \lim_{\varepsilon\to 0} D\delta(\varepsilon)\coth(\delta(\varepsilon)l)e^{\varepsilon t} \\ & - \frac{2D^2}{l^3}\sum_{n=1}^{+\infty}\frac{(n\pi)^2}{z_n}H(t)e^{z_nt}\end{aligned} \tag{A-19}$$

The first term in the right hand side of equation A-19 could be easily calculated from respective definitions of $\delta(s)$ and Pe as

$$\lim_{\varepsilon\to 0} D\delta(\varepsilon)\coth(\delta(\varepsilon)l)e^{\varepsilon t} = \frac{U}{2}\coth\left(\frac{Pe}{2}\right) \tag{A-20}$$

A.4 Pore concentration in the time domain

Piecewise application of Laplace inversion into equation A-2 leads to

$$\begin{aligned} V_i \mathscr{L}^{-1}\left(\overline{C_i}(s)\right) = &\sum_{j^+} e^{\frac{Pe}{2}} S(l) \mathscr{L}^{-1}\left(\mathrm{I}(s)\overline{C_j}(s)\right) \\ &+ \sum_{j^-} e^{-\frac{Pe}{2}} S(0) \mathscr{L}^{-1}\left(\mathrm{I}(s)\overline{C_j}(s)\right) \\ &- \sum_{j^+} S(l) \mathscr{L}^{-1}\left(\mathrm{II}(s)\overline{C_i}(s)\right) \\ &- \sum_{j^-} S(0) \mathscr{L}^{-1}\left(\mathrm{II}(s)\overline{C_i}(s)\right) \end{aligned} \tag{A-21}$$

One of the very significant properties possessed by the Laplace transform in connection with the convolution is that the Laplace transform of the convolution of two functions is the product of their Laplace transforms (Schiff, 1999). Hence, by applying the convolution Theorem the other way around one gets the following relationships

$$\mathscr{L}^{-1}\left(\mathrm{I}(s)\overline{C_j}(s)\right)(t) = \left[\mathscr{L}^{-1}\left(\mathrm{I}(s)\right) * C_j\right](t) \tag{A-22a}$$

$$\mathscr{L}^{-1}\left(\mathrm{II}(s)\overline{C_i}(s)\right)(t) = \left[\mathscr{L}^{-1}\left(\mathrm{II}(s)\right) * C_i\right](t) \tag{A-22b}$$

Insertion of equations A-22a and A-22b into equation A-21 results into the following expression

$$\begin{aligned} V_i C_i(t) = &\sum_{j^+} e^{\frac{Pe}{2}} S(l) \left(K^I * C_j\right)(t) \\ &+ \sum_{j^-} e^{-\frac{Pe}{2}} S(0) \left(K^I * C_j\right)(t) \\ &- \left(\left[\sum_{j^+} S(l) K^{II} + \sum_{j^-} S(0) K^{II}\right] * C_i\right)(t) \end{aligned} \tag{A-23}$$

where the convolution kernels, K^I and K^{II}, are nothing than inverse Laplace transforms of $\mathrm{I}(s)$ and $\mathrm{II}(s)$ whose final expressions result from insertion of equations A-18 and A-20 into equations A-17 and A-19, respectively. Thus

$$K^I(t) = \frac{U}{2\sinh\left(\frac{Pe}{2}\right)} - \frac{2D^2}{l^3}\sum_{n=1}^{+\infty}\frac{(-1)^n(n\pi)^2}{z_n}e^{z_n t} \tag{A-24a}$$

$$K^{II}(t) = \frac{U}{2}\coth\left(\frac{Pe}{2}\right) - \frac{2D^2}{l^3}\sum_{n=1}^{+\infty}\frac{(n\pi)^2}{z_n}e^{z_n t} \tag{A-24b}$$

Notice that these two convolution kernel functions contain a time-independent term which is expected to play a major role for the asymptotic concentration $\hat{C}_i$ at network node i. The remaining time-dependent terms are given in the form of exponentially decreasing and convergent series. These convolution kernels are throat related because they're convoluted with upstream (i.e. C_{j^+}) and downstream (i.e. C_{j^-}) in throats connected to pore i. These functions depend solely on the local characteristics of pore channels, namely their length, diffusivity, and fluid velocity.

We further define a surface-area weighted kernel function

$$\tilde{K}^{II}(t) = \sum_{j^+} S(l) K^{II}(t) + \sum_{j^-} S(0) K^{II}(t) \tag{A-25}$$

Notice that $\tilde{K}^{II}$ appearing in equation A-25 is a pore related function because it is convoluted with average time-dependent concentrations at a node i of the network as shown in equation A-23. Finally, substitution of equations A-24a, A-24b, and A-25 into A-23 leads to an equation describing concentration evolution in each pore as a linear convolution with average concentrations in neighbour pores as

$$\begin{aligned} V_i C_i(t) = & \sum_{j^+} e^{\frac{Pe}{2}} S(l) \left(K^I * C_j\right)(t) \\ & + \sum_{j^-} e^{-\frac{Pe}{2}} S(0) \left(K^I * C_j\right)(t) \\ & - \left(\tilde{K}^{II} * C_i\right)(t) \end{aligned} \tag{A-26}$$

The convolution kernels given by equations A-24a and A-24b are Péclet- and time- dependent functions of interconnected throats.

Equation A-26 is only valid for internal pores which are not directly connected to inflow or outflow boundaries. In such cases, other formulas are derived by simple adjustment of the previous expression following the same procedure. For inflowing pores the following expression is rather obtained

$$\begin{aligned} V_i C_i(t) = & \sum_{j^+} J_j^{in} S(l) t \\ & + \sum_{j^-} e^{-\frac{Pe}{2}} S(0) \left(K^I * C_j\right)(t) \\ & - \sum_{j^-} \left(S(0) K^{II} * C_i\right)(t) \end{aligned} \tag{A-27}$$

where J_j^{in} is a fixed external mass flux associated to inflowing throat j located upstream to pore i.

Similarly, mass conservation on pores at the outflow boundary implies the following relationship

$$\begin{aligned} V_i C_i(t) = & \sum_{j^-} Q_j^{out} C_i(t) t \\ & + \sum_{j^+} e^{\frac{Pe}{2}} S(l) \left(K^I * C_j\right)(t) \\ & - \sum_{j^+} \left(S(l) K^{II} * C_i\right)(t) \end{aligned} \tag{A-28}$$

Appendix B Inverse Laplace transform of concentrations in throats

To invert equation 23 back into the time domain we follow the same methodology exposed in Appendix A. First, the equation is regularized in Laplace space through a division by s such that

$$\frac{\overline{C}(\xi, s)}{s} = e^{\frac{U\xi}{2D}} \frac{\sinh\left(\delta(l-\xi)\right)}{s \sinh\left(\delta l\right)} \overline{C}_{\xi_1}(s) + e^{\frac{-U(l-\xi)}{2D}} \frac{\sinh\left(\delta\xi\right)}{s \sinh\left(\delta l\right)} \overline{C}_{\xi_2}(s) \tag{B-1}$$

We identify two terms in the last equation which necessitate separate Laplace inversion, namely $\mathrm{III}(s) = \frac{\sinh(\delta(l-\xi))}{s\sinh(\delta l)}$ and $\mathrm{IV}(s) = \frac{\sinh(\delta\xi)}{s\sinh(\delta l)}$.

B.1 Inverse Laplace expression of the term III(s)

Here again the conjunctive use of Euler's formula for the hyperbolic sine function and the partial fraction expansion technique for the complex sine function as used earlier to derive equation A-6 leads to the following equality

$$\mathrm{III}(s) = \frac{\sinh\left(\delta(l-\xi)\right)}{s}\left(1 + 2\sum_{n=1}^{+\infty}\frac{(-1)^n(\delta l)^2}{(n\pi)^2 + (\delta l)^2}\right) \tag{B-2}$$

by analogy to preceding developments in Appendix A and by noting that $\delta(z_n)l = in\pi$, we can get the residue at pole z_n as

$$Res\left(\mathrm{III}(s)e^{st}, z_n\right) = \frac{2D}{l^2}\frac{1}{z_n}\left[(-1)^n(ni\pi)\sinh\left(\frac{ni\pi}{l}(l-\xi)\right)\right]e^{z_n t} \tag{B-3}$$

which could to be simplified to

$$Res\left(\mathrm{III}(s)e^{st}, z_n\right) = \frac{2D}{l^2}\frac{1}{z_n}n\pi\sin\left(n\pi\frac{\xi}{l}\right)e^{z_n t} \tag{B-4}$$

the residue at the limit $\varepsilon \to 0$ is equally calculated as

$$\lim_{\varepsilon\to 0} Res\left(\mathrm{III}(s)e^{st}, \varepsilon\right) = \frac{\sinh\left(\frac{U(l-\xi)}{2D}\right)}{\sinh\left(\frac{Ul}{2D}\right)} \tag{B-5}$$

592 ### B.2 Inverse Laplace expression of the term IV(s)

by analogy to the previous expression the residue at pole z_n is given by

$$Res\left(\mathrm{IV}(s)e^{st}, z_n\right) = \frac{2D}{l^2}\frac{1}{z_n}\left[(-1)^n(ni\pi)\sinh\left(ni\pi\frac{\xi}{l}\right)\right]e^{z_n t} \tag{B-6}$$

which is readily simplified to

$$Res\left(\mathrm{IV}(s)e^{st}, z_n\right) = \frac{2D}{l^2}\frac{1}{z_n}(-1)^{n+1}n\pi\sin\left(n\pi\frac{\xi}{l}\right)e^{z_n t} \tag{B-7}$$

the residue at the limit $\varepsilon \to 0$ is

$$\lim_{\varepsilon\to 0} Res\left(\mathrm{VI}(s)e^{st}, \varepsilon\right) = \frac{\sinh\left(\frac{U\xi}{2D}\right)}{\sinh\left(\frac{Ul}{2D}\right)} \tag{B-8}$$

593 ### B.3 Inverse Laplace transform expressions of III(s) and IV(s)

Application of the residue Theorem to the two functions III(s) and IV(s) terms allow to calculate their inverse Laplace transforms as

$$\begin{aligned}\mathscr{L}^{-1}\left(III(s)\right)(t) = &\frac{\sinh\left(\frac{U(l-\xi)}{2D}\right)}{\sinh\left(\frac{Ul}{2D}\right)} \\ &+ \frac{2D}{l^2}\sum_{n=1}^{+\infty}\sin\left(n\pi\frac{\xi}{l}\right)\frac{n\pi}{z_n}e^{z_n t}\end{aligned} \tag{B-9}$$

and

$$\begin{aligned}\mathscr{L}^{-1}\left(IV(s)\right)(t) = &\frac{\sinh\left(\frac{U\xi}{2D}\right)}{\sinh\left(\frac{Ul}{2D}\right)} \\ &- \frac{2D}{l^2}\sum_{n=1}^{\infty}(-1)^n\sin\left(n\pi\frac{\xi}{l}\right)\frac{n\pi}{z_n}e^{z_n t}\end{aligned} \tag{B-10}$$

B.4 Throat concentration in the time domain

Because $\mathscr{L}^{-1}\left(\frac{\bar{f}(s)}{s}\right) = \int_0^t f(\tau)\, d\tau$, the expected convolution kernels involved in the time-dependent concentration along a throat are obtained from first-order derivatives of equations B-9 and B-10, respectively. The final relationship is given as

$$C(\xi,t) = K_l^I(\xi,t) * C_{\xi_1}(t) + K_l^{II}(\xi,t) * C_{\xi_2}(t) \tag{B-11}$$

where the space and time dependent kernel functions are

$$K_l^I(\xi,t) = -\frac{2D}{l^2} e^{\frac{U\xi}{2D}} \sum_{n=1}^{+\infty} (-1)^n \sin\left(n\pi\frac{\xi}{l}\right) n\pi e^{z_n t} \tag{B-12a}$$

$$K_l^{II}(\xi,t) = -\frac{2D}{l^2} e^{-\frac{U(l-\xi)}{2D}} \sum_{n=1}^{+\infty} (-1)^n \sin\left(n\pi\frac{l-\xi}{l}\right) n\pi e^{z_n t} \tag{B-12b}$$

Appendix C Asymptotic pore concentration

To derive the asymptotic form of equation A-26, we let the characteristic diffusion time t_{diff} going to zero while keeping Pe constant. In this limit, the convolution kernels given by equations A-24a and A-24b reduce to their first constant terms. This leads to

$$\begin{aligned} V_i\hat{C}_i(t) = &\sum_{j^+} e^{\frac{Pe}{2}} S(l) \frac{U}{2\sinh\left(\frac{Pe}{2}\right)} \int_0^t \hat{C}_j(\tau)d\tau \\ &+ \sum_{j^-} e^{\frac{-Pe}{2}} S(0) \frac{U}{2\sinh\left(\frac{Pe}{2}\right)} \int_0^t \hat{C}_j(\tau)d\tau \\ &- \sum_{j} \frac{1}{2} S \coth\left(\frac{Pe}{2}\right) \int_0^t \hat{C}_i(\tau)d\tau \end{aligned} \tag{C-1}$$

Differentiating equation C-1 gives the asymptotic ODE form of the mass balance equation

$$\begin{aligned} V_i\frac{d\hat{C}_i}{dt} = &\sum_{j^+} US(l)\frac{e^{\frac{Pe}{2}}}{2\sinh\left(\frac{Pe}{2}\right)}\hat{C}_j + \sum_{j^-} US(0)\frac{e^{\frac{-Pe}{2}}}{2\sinh\left(\frac{Pe}{2}\right)}\hat{C}_j \\ &- \sum_{j} \frac{1}{2} US \coth\left(\frac{Pe}{2}\right)\hat{C}_i \end{aligned} \tag{C-2}$$

C.1 Asymptotic behavior as Pe→ $+\infty$

To study the behavior of the asymptotic mass balance scheme given by equation C-2 when Pe→ $+\infty$ we note that

$$\lim_{Pe\to+\infty} \frac{e^{\frac{Pe}{2}}}{2\sinh\left(\frac{Pe}{2}\right)} = 1 \tag{C-3a}$$

$$\lim_{Pe\to+\infty} \frac{e^{\frac{-Pe}{2}}}{2\sinh\left(\frac{Pe}{2}\right)} = 0 \tag{C-3b}$$

$$\lim_{Pe\to+\infty} \coth\left(\frac{Pe}{2}\right) = 1 \tag{C-3c}$$

Substituting equations C-3a-C-3c into equation C-2 leads to

$$V_i\frac{d\hat{C}_i}{dt} = \sum_{j^+} US(l)\hat{C}_j - \frac{1}{2}\left[\sum_{j^+} US(l) + \sum_{j^-} US(0)\right]\hat{C}_i \tag{C-4}$$

Because the fluid is incompressible (i.e. $\sum_{j^+} US(l) = \sum_{j^-} US(0)$), the last term in the previous equation equals to $\sum_{j^-} US(0)\hat{C}_i$. Hence, the behavior of our asymptotic mass balance formulation for high Péclet numbers regime (i.e. advection dominant regime) is identical to the MCM mass balance formulation given by equation 34 with $C_x = C_i$.

C.2 Asymptotic behavior as Pe$\rightarrow$ 0

Similarly, to study behavior of the asymptotic mass balance scheme given by equation C-2 when Pe$\rightarrow$ 0, we rewrite the two first terms in its right-hand side as

$$e^{\frac{Pe}{2}} \frac{U}{2\sinh\left(\frac{Pe}{2}\right)} = \frac{Pe}{2\sinh\left(\frac{Pe}{2}\right)} \frac{D}{l} e^{\frac{Pe}{2}} \tag{C-5a}$$

$$e^{\frac{-Pe}{2}} \frac{U}{2\sinh\left(\frac{Pe}{2}\right)} = \frac{Pe}{2\sinh\left(\frac{Pe}{2}\right)} \frac{D}{l} e^{\frac{-Pe}{2}} \tag{C-5b}$$

and because

$$\lim_{Pe\rightarrow 0} \frac{Pe}{2\sinh\left(\frac{Pe}{2}\right)} = 1 \tag{C-6a}$$

$$\lim_{Pe\rightarrow 0} e^{\frac{Pe}{2}} \approx 1 + \frac{Pe}{2} \tag{C-6b}$$

$$\lim_{Pe\rightarrow 0} e^{\frac{-Pe}{2}} \approx 1 - \frac{Pe}{2} \tag{C-6c}$$

$$\lim_{Pe\rightarrow 0} \frac{1}{2}\coth\left(\frac{Pe}{2}\right) \approx \frac{1}{Pe} \tag{C-6d}$$

Insertion of equations C-5a-C-5b into equation C-2, and direct application of the relationships given by equations C-6a-C-6d, leads to

$$\begin{aligned} V_i \frac{d\hat{C}_i}{dt} &= \sum_{j^+} \frac{1}{2} US(l)\hat{C}_j - \sum_{j^-} \frac{1}{2} US(0)\hat{C}_j \\ &+ \sum_{j^+} \frac{D}{l} S(l)(\hat{C}_j - \hat{C}_i) + \sum_{j^-} \frac{D}{l} S(0)(\hat{C}_j - \hat{C}_i) \end{aligned} \tag{C-7}$$

Because $U \ll \frac{D}{l}$ we can subsequently conclude that $\sum_{j^+} \frac{1}{2} US(l)\hat{C}_j - \sum_{j^-} \frac{1}{2} US(0)\hat{C}_j \ll \sum_j \frac{D}{l} S(\hat{C}_j - \hat{C}_i)$. Hence, the behavior of our asymptotic mass balance formulation for low Péclet numbers (i.e. diffusion dominant regime) is the so-called CD-MCM mass balance formulation given by equation 34 with $C_x = C_j$ and $U_{ij} = \frac{U}{2}$. Notably, the MCM scheme given in equation 34 do not take into account the mass in the throats explaining this difference.

Appendix D Asymptotic throat concentration

The asymptotic concentration regime in a throat is obtained from equation B-11 when t_{diff} goes to zero while Pe is kept constant, such that

$$\hat{C}(\xi) = \hat{K}_l^I(\xi)\hat{C}_{\xi_1} + \hat{K}_l^{II}(\xi)\hat{C}_{\xi_2} \tag{D-1}$$

where

$$\hat{K}_l^I(\xi) = e^{\frac{Pe\xi}{2l}} \frac{\sinh\left(\frac{Pe(l-\xi)}{2l}\right)}{\sinh\left(\frac{Pe}{2}\right)} \tag{D-2a}$$

$$\hat{K}_l^{II}(\xi) = e^{-\frac{Pe(l-\xi)}{2l}} \frac{\sinh\left(\frac{Pe\xi}{2l}\right)}{\sinh\left(\frac{Pe}{2}\right)} \tag{D-2b}$$

Using the equality

$$-2\sum_{n=1}^{\infty}\frac{(-1)^n\sin(n\pi\xi)}{n^2\pi^2+Pe^2/4}=\frac{\sinh(\frac{Pe}{2}\xi)}{\sinh(\frac{Pe}{2})} \tag{D-3}$$

It's quite easy to verify that the sum of asymptotic kernel functions $\hat{K}_l^I$ and $\hat{K}_l^{II}$ is unity anywhere along ξ-axis

$$\hat{K}_l^I(\xi)+\hat{K}_l^{II}(\xi)=1 \tag{D-4}$$

Finally, by inserting equation D-4 into equation D-1, the asymptotic concentration profile along the throat is uniquely dependent on concentrations in neighbor pores and Péclet number(through $\hat{K}_l^I$ given by equation D-2a). It is given as follows

$$\hat{C}(\xi)=\hat{C}_{\xi_2}-\hat{K}_l^I(\xi)\left(\hat{C}_{\xi_2}-\hat{C}_{\xi_1}\right) \tag{D-5}$$

A direct consequence of equation D-5 is that the long-term concentration profiles inside network throats satisfy the maximum discrete principle, that is

$$\min\left(\hat{C}_{\xi_1},\hat{C}_{\xi_2}\right)\leq\hat{C}(\xi)\leq\max\left(\hat{C}_{\xi_1},\hat{C}_{\xi_2}\right) \tag{D-6}$$

Data Availability Statement

Data is available through Øren and Bakke (2002) and Øren and Bakke (2003).

References

Acharya, R. C., der Zee], S. V., & Leijnse, A. (2005). Transport modeling of nonlinearly adsorbing solutes in physically heterogeneous pore networks. *Water Resources Research*, *41*(2). doi: 10.1029/2004WR003500

Acharya, R. C., der Zee], S. V., & Leijnse, A. (2007). Approaches for modeling longitudinal dispersion in pore-networks. *Advances in Water Resources*, *30*(2), 261 - 272. doi: https://doi.org/10.1016/j.advwatres.2005.11.015

Algive, L., Békri, S., & Vizika, O. (2010). Pore-network modeling dedicated to the determination of the petrophysical-property changes in the presence of reactive fluid. *SPE Journal*, *15*(3), 618-633. doi: 10.2118/124305-PA

Alvarado, V., Davis, H., & Scriven, L. (1997). Effects of pore-level reaction on dispersion in porous media. *Chemical Engineering Science*, *52*(17), 2865 - 2881. doi: https://doi.org/10.1016/S0009-2509(97)00100-0

Anderson, M. P., & Cherry, J. A. (1979). Using models to simulate the movement of contaminants through groundwater flow systems. *C R C Critical Reviews in Environmental Control*, *9*(2), 97-156. doi: 10.1080/10643387909381669

Aris, R., & Taylor, G. I. (1956). On the dispersion of a solute in a fluid flowing through a tube. *Proceedings of the Royal Society of London. Series A. Mathematical and Physical Sciences*, *235*(1200), 67-77. doi: 10.1098/rspa.1956.0065

Bastian, P., Engwer, C., Fahlke, J., & Ippisch, O. (2011). An unfitted discontinuous galerkin method for pore-scale simulations of solute transport. *Mathematics and Computers in Simulation*, *81*(10), 2051 - 2061. doi: https://doi.org/10.1016/j.matcom.2010.12.024

Bear, J. (1972). *Dynamics of Fluids in Porous Media.* New York: Elsevier.

Bear, J., & Cheng, A. H. D. (2010). *Modeling Groundwater Flow and Contaminant Transport.* Dordrecht, the Netherlands: Springer.

Bijeljic, B., Muggeridge, A. H., & Blunt, M. J. (2004). Pore-scale modeling of longitudinal dispersion. *Water Resources Research*, *40*(11). doi: 10.1029/2004WR003567

Blunt, M. J. (2001). Flow in porous media — pore-network models and multiphase flow. *Current Opinion in Colloid & Interface Science*, *6*(3), 197 - 207. doi: https://doi.org/10.1016/S1359-0294(01)00084-X

Blunt, M. J., Bijeljic, B., Dong, H., Gharbi, O., Iglauer, S., Mostaghimi, P., ... Pentland, C. (2013). Pore-scale imaging and modelling. *Advances in Water Resources*, *51*, 197 - 216. doi: https://doi.org/10.1016/j.advwatres.2012.03.003

Budek, A., & Szymczak, P. (2012). Network models of dissolution of porous media. *Physical Review E*, *86*, 056318. doi: 10.1103/PhysRevE.86.056318

Chen, S., & Doolen, G. D. (1998). Lattice Boltzmann method for fluid flows. *Annual Review of Fluid Mechanics*, *30*(1), 329-364. doi: 10.1146/annurev.fluid.30.1.329

Davis, T. A. (2004). Algorithm 832: UMFPACK V4.3—an unsymmetric-pattern multifrontal method. *ACM Transactions in Mathematical Software*, *30*(2), 196–199. doi: 10.1145/992200.992206

de Arcangelis, L., Koplik, J., Redner, S., & Wilkinson, D. (1986). Hydrodynamic dispersion in network models of porous media. *Physical Review Letters*, *57*, 996–999. doi: 10.1103/PhysRevLett.57.996

Dillard, L. A., & Blunt, M. J. (2000). Development of a pore network simulation model to study nonaqueous phase liquid dissolution. *Water Resources Research*, *36*(2), 439-454. doi: 10.1029/1999WR900301

Dormand, J., & Prince, P. (1986). Runge-kutta triples. *Computers & Mathematics with Applications*, *12*(9, Part A), 1007 - 1017. doi: 10.1016/0898-1221(86)90025-8

Dullien, F. A. L. (1992). *Porous Media: Fluid Transport and Pore Structure (2nd Edition)*. San Diego: Academic Press.

Fatt, I. (1956a). The network model of porous media I. Capillary characteristics. *Transactions of the AIME*, *207*(1), 144-159.

Fatt, I. (1956b). The network model of porous media II. Dynamic properties of a single size tube network. *Transactions of the AIME*, *207*(1), 160-163.

Fatt, I. (1956c). The network model of porous media III. Dynamic properties of networks with tube radius distribution. *Transactions of the AIME*, *207*(1), 164-181.

Fredd, C. N., & Fogler, H. S. (1998). Influence of transport and reaction on wormhole formation in porous media. *AIChE Journal*, *44*(9), 1933-1949. doi: 10.1002/aic.690440902

Gelhar, L. W., Welty, C., & Rehfeldt, K. R. (1992). A critical review of data on field-scale dispersion in aquifers. *Water Resources Research*, *28*(7), 1955-1974. doi: 10.1029/92WR00607

Icardi, M., Boccardo, G., Marchisio, D. L., Tosco, T., & Sethi, R. (2014). Pore-scale simulation of fluid flow and solute dispersion in three-dimensional porous media. *Physical Review E*, *90*, 013032. doi: 10.1103/PhysRevE.90.013032

Kamtchueng, T. (2016). *A Generalized Formulation for Reactive Transport in Pore Network Models in Saturated Media (In French)* (Unpublished doctoral dissertation). Université d'Orléans, Orléans.

Kim, D., Peters, C. A., & Lindquist, W. B. (2011). Upscaling geochemical reaction rates accompanying acidic CO2-saturated brine flow in sandstone aquifers. *Water Resources Research*, *47*(1). doi: 10.1029/2010WR009472

Laudone, G., Matthews, G., Bird, N., Whalley, W., Cardenas, L., & Gregory, A. (2011). A model to predict the effects of soil structure on denitrification and N2O emission. *Journal of Hydrology*, *409*(1), 283 - 290. doi: https://doi.org/10.1016/j.jhydrol.2011.08.026

Li, L., Peters, C. A., & Celia, M. A. (2006). Upscaling geochemical reaction rates using pore-scale network modeling. *Advances in Water Resources*, *29*(9), 1351 - 1370. doi: https://doi.org/10.1016/j.advwatres.2005.10.011

Li, L., Steefel, C. I., & Yang, L. (2008). Scale dependence of mineral dissolution rates within single pores and fractures. *Geochimica et Cosmochimica Acta*, *72*(2), 360 - 377. doi: https://doi.org/10.1016/j.gca.2007.10.027

Li, S., Raoof, A., & Schotting, R. (2014). Solute dispersion under electric and pressure driven flows; pore scale processes. *Journal of Hydrology*, *517*, 1107 - 1113. doi: https://doi.org/10.1016/j.jhydrol.2014.06.049

Martins, A. A., Laranjeira, P. E., Braga, C. H., & Mata, T. M. (2009). Modeling of transport phenomena in porous media using network models. In *Progress in porous media research* (p. 156-261). New York: Nova Science Publishers.

Mason, G., & Morrow, N. R. (1991). Capillary behavior of a perfectly wetting liquid in irregular triangular tubes. *Journal of Colloid and Interface Science*, *141*(1), 262 - 274. doi: https://doi.org/10.1016/0021-9797(91)90321-X

Mehmani, Y., & Balhoff, M. T. (2015a). Eulerian network modeling of longitudinal dispersion. *Water Resources Research*, *51*(10), 8586-8606. doi: 10.1002/2015WR017543

Mehmani, Y., & Balhoff, M. T. (2015b). Mesoscale and Hybrid Models of Fluid Flow and Solute Transport. *Reviews in Mineralogy and Geochemistry*, *80*(1), 433-459. doi: 10.2138/rmg.2015.80.13

Mehmani, Y., Oostrom, M., & Balhoff, M. T. (2014). A streamline splitting pore-network approach for computationally inexpensive and accurate simulation of transport in porous media. *Water Resources Research*, *50*(3), 2488-2517. doi: 10.1002/2013WR014984

Mehmani, Y., Sun, T., Balhoff, M. T., Eichhubl, P., & Bryant, S. (2012). Multi-block pore-scale modeling and upscaling of reactive transport: Application to carbon sequestration. *Transport in Porous Media*, *95*(2), 305-326. doi: 10.1007/s11242-012-0044-7

Miller, C. T., Dawson, C. N., Farthing, M. W., Hou, T. Y., Huang, J., Kees, C. E., ... Langtangen, H. P. (2013). Numerical simulation of water resources problems: Models, methods, and trends. *Advances in Water Resources*, *51*, 405 - 437. doi: https://doi.org/10.1016/j.advwatres.2012.05.008

Milligen, B. P. V., & Bons, P. (2014). Simplified numerical model for clarifying scaling behavior in the intermediate dispersion regime in homogeneous porous media. *Computer Physics Communications*, *185*(12), 3291 - 3301. doi: https://doi.org/10.1016/j.cpc.2014.09.006

Molins, S. (2015). Reactive interfaces in direct numerical simulation of pore-scale processes. *Reviews in Mineralogy and Geochemistry*, *80*(1), 461-481. doi: 10.2138/rmg.2015.80.14

Molins, S., Trebotich, D., Steefel, C. I., & Shen, C. (2012). An investigation of the effect of pore scale flow on average geochemical reaction rates using direct numerical simulation. *Water Resources Research*, *48*(3). doi: 10.1029/2011WR011404

Monaghan, J. J. (1992). Smoothed particle hydrodynamics. *Annual Review of Astronomy and Astrophysics*, *30*(1), 543-574. doi: 10.1146/annurev.aa.30.090192.002551

Mostaghimi, P., Bijeljic, B., & Blunt, M. J. (2012). Pore-scale simulation of fluid flow and solute dispersion in three-dimensional porous media. *SPE Journal*, *17*(4). doi: 10.2118/135261-MS

Neuman, S. P. (1990). Universal scaling of hydraulic conductivities and dispersivities in geologic media. *Water Resources Research*, *26*(8), 1749-1758. doi: 10.1029/WR026i008p01749

Oostrom, M., Mehmani, Y., Romero-Gomez, P., Tang, Y., Liu, H., Yoon, H., ... Zhang, C. (2016). Pore-scale and continuum simulations of solute transport micromodel benchmark experiments. *Computational Geosciences*, *20*(4), 857 - 879. doi: 10.1007/s10596-014-9424-0

Owen, J. E. (1952). The resistivity of a fluid-filled porous body. *Journal of Petroleum Technology*, *4*(7), 169-174.

Patzek, T., & Silin, D. (2001). Shape factor and hydraulic conductance in noncircular capillaries: I. one-phase creeping flow. *Journal of Colloid and Interface Science*, *236*(2), 295 - 304. doi: https://doi.org/10.1006/jcis.2000.7413

Pickens, J. F., & Grisak, G. E. (1981). Scale-dependent dispersion in a stratified granular aquifer. *Water Resources Research*, *17*(4), 1191-1211. doi: 10.1029/WR017i004p01191

Piri, M., & Blunt, M. J. (2005a). Three-dimensional mixed-wet random pore-scale network modeling of two- and three-phase flow in porous media. II. Results. *Physical Review E*, *71*(2), 026302. doi: 10.1103/PhysRevE.71.026302

Piri, M., & Blunt, M. J. (2005b). Three-dimensional mixed-wet random pore-scale network modeling of two- and three-phase flow in porous media. I. Model description. *Physical Review E*, *71*(2), 026301. doi: 10.1103/PhysRevE.71.026301

Qin, C.-Z., Hassanizadeh, S. M., & Ebigbo, A. (2016). Pore-scale network modeling of microbially induced calcium carbonate precipitation: Insight into scale dependence of biogeochemical reaction rates. *Water Resources Research*, *52*(11), 8794-8810. doi: 10.1002/2016WR019128

Raeini, A. Q., Bijeljic, B., & Blunt, M. J. (2015). Modelling capillary trapping using finite-volume simulation of two-phase flow directly on micro-CT images. *Advances in Water Resources*, *83*, 102 - 110. doi: https://doi.org/10.1016/j.advwatres.2015.05.008

Raeini, A. Q., Blunt, M. J., & Bijeljic, B. (2014). Direct simulations of two-phase flow on micro-CT images of porous media and upscaling of pore-scale forces. *Advances in Water Resources*, *74*, 116 - 126. doi: https://doi.org/10.1016/j.advwatres.2014.08.012

Raoof, A., Nick, H., Hassanizadeh, S., & Spiers, C. (2013). Poreflow: A complex pore-network model for simulation of reactive transport in variably saturated porous media. *Computers & Geosciences*, *61*, 160 - 174. doi: https://doi.org/10.1016/j.cageo.2013.08.005

Raoof, A., Nick, H., Wolterbeek, T., & Spiers, C. (2012). Pore-scale modeling of reactive transport in wellbore cement under CO2 storage conditions. *International Journal of Greenhouse Gas Control*, *11*, S67 - S77. doi: https://doi.org/10.1016/j.ijggc.2012.09.012

Øren, P.-E., & Bakke, S. (2002). Process based reconstruction of sandstones and prediction of transport properties. *Transport in Porous Media*, *46*(2), 311-343. doi: 10.1023/A:1015031122338

Øren, P.-E., & Bakke, S. (2003). Reconstruction of Berea sandstone and pore-scale modelling of wettability effects. *Journal of Petroleum Science and Engineering*, *39*(3), 177 - 199. doi: https://doi.org/10.1016/S0920-4105(03)00062-7

Saad, Y. (2003). *Iterative Methods for Sparse Linear Systems (2nd edition)*. Philadelphia, Pasadena: SIAM.

Sadeghi, M. A., Agnaou, M., Barralet, J., & Gostick, J. (2020). Dispersion modeling in pore networks: A comparison of common pore-scale models and alternative approaches. *Journal of Contaminant Hydrology*, *228*, 103578. doi: https://doi.org/10.1016/j.jconhyd.2019.103578

Sahimi, M., Davis, H. T., & Scriven, L. E. (1983). Dispersion in disordered porous media. *Chemical Engineering Communications*, *23*(4-6), 329-341. doi: 10.1080/00986448308940483

Sahimi, M., Hughes, B. D., Scriven, L., & Davis, H. T. (1986). Dispersion in flow through porous media—i. one-phase flow. *Chemical Engineering Science*, *41*(8), 2103 - 2122. doi: https://doi.org/10.1016/0009-2509(86)87128-7

Scheidegger, A. E. (1974). *The Physics of Flow Through Porous Media (3rd Edition)*. University of Toronto Press.

Schiff, J. L. (1999). *The Laplace Transform: Theory and Applications*. New York: Springer-Verlag.

Schulze-Makuch, D. (2005). Longitudinal dispersivity data and implications for scaling behavior. *Groundwater*, *43*(3), 443-456. doi: 10.1111/j.1745-6584.2005.0051.x

Shampine, L., & Thompson, S. (2001). Solving ddes in matlab. *Applied Numerical Mathematics*, *37*(4), 441 - 458. doi: 10.1016/S0168-9274(00)00055-6

Sharma, M. M., & Yortsos, Y. C. (1987). A network model for deep bed filtration processes. *AIChE Journal*, *33*(10), 1644-1653. doi: 10.1002/aic.690331008

Silliman, S. E., Konikow, L. F., & Voss, C. I. (1987). Laboratory investigation of longitudinal dispersion in anisotropic porous media. *Water Resources Research*, *23*(11), 2145-2151. doi: 10.1029/WR023i011p02145

Silliman, S. E., & Simpson, E. S. (1987). Laboratory evidence of the scale effect in dispersion of solutes in porous media. *Water Resources Research*, *23*(8), 1667-1673. doi: 10.1029/WR023i008p01667

Song, Y.-Q., Cho, H., Hopper, T., Pomerantz, A. E., & Sun, P. Z. (2008). Magnetic resonance in porous media: Recent progress. *The Journal of Chemical Physics*, *128*(5), 052212. doi: 10.1063/1.2833581

Sorbie, K., & Clifford, P. (1991). The inclusion of molecular diffusion effects in the network modelling of hydrodynamic dispersion in porous media. *Chemical Engineering Science*, *46*(10), 2525 - 2542. doi: https://doi.org/10.1016/0009-2509(91)80046-2

Steefel, C. I., & MacQuarrie, K. T. B. (1996). Approaches to modeling of reactive transport in porous media. In P. C. Lichtner, C. I. Steefel, & E. H. Oelkers (Eds.), *Reactive Transport in Porous Media* (Vol. 34, p. 83-129). Washington, DC: Mineralogical Society of America.

Stehfest, H. (1970). Algorithm 368: Numerical inversion of Laplace transforms [D5]. *ACM Communications*, *13*(1), 47–49. doi: 10.1145/361953.361969

Suchomel, B. J., Chen, B. M., & Allen, M. B. (1998). Network model of flow transport and biofilm effects in porous media. *Transport in Porous Media*, *30*(1), 1-23. doi: 10.1023/A:1006560705680

Sudicky, E. A., Gillham, R. W., & Frind, E. O. (1985). Experimental investigation of solute transport in stratified porous media: 1. the nonreactive case. *Water Resources Research*, *21*(7), 1035-1041. doi: 10.1029/WR021i007p01035

Tansey, J., & Balhoff, M. T. (2016). Pore network modeling of reactive transport and dissolution in porous media. *Transport in Porous Media*, *113*(2), 303-327. doi: 10.1007/s11242-016-0695-x

Tartakovsky, A. M., & Meakin, P. (2006). Pore scale modeling of immiscible and miscible fluid flows using smoothed particle hydrodynamics. *Advances in Water Resources*, *29*(10), 1464 - 1478. doi: https://doi.org/10.1016/j.advwatres.2005.11.014

Tartakovsky, A. M., Tartakovsky, D. M., Scheibe, T. D., & Meakin, P. (2008). Hybrid simulations of reaction-diffusion systems in porous media. *SIAM Journal on Scientific Computing*, *30*(6), 2799-2816. doi: 10.1137/070691097

Taylor, G. I. (1953). Dispersion of soluble matter in solvent flowing slowly through a tube. *Proceedings of the Royal Society of London. Series A. Mathematical and Physical Sciences*, *219*(1137), 186-203. doi: 10.1098/rspa.1953.0139

Thullner, M., & Baveye, P. (2008). Computational pore network modeling of the influence of biofilm permeability on bioclogging in porous media. *Biotechnology and bioengineering*, *99*(6), 1337-1351. doi: 10.1002/bit.21708

Trebotich, D., Adams, M. F., Molins, S., Steefel, C. I., & Shen, C. (2014). High-resolution simulation of pore-scale reactive transport processes associated with carbon sequestration. *Computing in Science and Engineering*, *16*(6), 22-31. doi: 10.1109/MCSE.2014.77

Valvatne, P. H., Piri, M., Lopez, X., & Blunt, M. J. (2002). Predictive pore-scale modeling of single and multiphase flow. *Transport in Porous Media*, *58*(1), 23-41. doi: 10.1007/s11242-004-5468-2

Varloteaux, C., Békri, S., & Adler, P. M. (2013). Pore network modelling to determine the transport properties in presence of a reactive fluid: From pore to reservoir scale. *Advances in Water Resources*, *53*, 87 - 100. doi:

https://doi.org/10.1016/j.advwatres.2012.10.004
Wang, Q., & Zhan, H. (2015). On different numerical inverse Laplace methods for solute transport problems. *Advances in Water Resources*, *75*, 80 - 92. doi: https://doi.org/10.1016/j.advwatres.2014.11.001
Wildenschild, D., & Sheppard, A. P. (2013). X-ray imaging and analysis techniques for quantifying pore-scale structure and processes in subsurface porous medium systems. *Advances in Water Resources*, *51*, 217 - 246. doi: 10.1016/j.advwatres.2012.07.018
Xiong, Q., Baychev, T. G., & Jivkov, A. P. (2016). Review of pore network modelling of porous media: Experimental characterisations, network constructions and applications to reactive transport. *Journal of Contaminant Hydrology*, *192*, 101 - 117. doi: 10.1016/j.jconhyd.2016.07.002
Xiong, Q., Joseph, C., Schmeide, K., & Jivkov, A. P. (2015). Measurement and modelling of reactive transport in geological barriers for nuclear waste containment. *Physical Chemistry Chemical Physics*, *17*, 30577-30589. doi: 10.1039/C5CP05243B
Yang, X., Mehmani, Y., Perkins, W. A., Pasquali, A., Schönherr, M., Kim, K., ... Scheibe, T. D. (2016). Intercomparison of 3D pore-scale flow and solute transport simulation methods. *Advances in Water Resources*, *95*, 176 - 189. doi: https://doi.org/10.1016/j.advwatres.2015.09.015
Yoon, H., Kang, Q., & Valocchi, A. J. (2015). Lattice Boltzmann-based approaches for pore-scale reactive transport. *Reviews in Mineralogy and Geochemistry*, *80*(1), 393-431. doi: 10.2138/rmg.2015.80.12
Zaretskiy, Y., Geiger, S., Sorbie, K., & Förster, M. (2010). Efficient flow and transport simulations in reconstructed 3d pore geometries. *Advances in Water Resources*, *33*(12), 1508 - 1516. doi: https://doi.org/10.1016/j.advwatres.2010.08.008
Zheng, C., & Bennett, G. D. (2002). *Applied Contaminant Transport Modeling (2nd Edition)*. New York: Wiley.